

1 **CMIP6/PMIP4 simulations of the mid-Holocene and Last Interglacial using**
2 **HadGEM3: comparison to the pre-industrial era, previous model versions,**
3 **and proxy data**

4
5 **Charles J. R. Williams^{1,5}, Maria-Vittoria Guarino², Emilie Capron³, Irene Malmierca-**
6 **Vallet^{1,2}, Joy S. Singarayer^{4,1}, Louise C. Sime², Daniel J. Lunt¹, Paul J. Valdes¹**

7
8 ¹School of Geographical Sciences, University of Bristol, UK (c.j.r.williams@bristol.ac.uk)

9 ²British Antarctic Survey, Cambridge, UK

10 ³Physics of Ice, Climate and Earth, Niels Bohr Institute, University of Copenhagen, Denmark

11 ⁴Department of Meteorology & School of Archaeology, Geography and Environmental
12 Science, University of Reading, UK

13 ⁵NCAS-Climate / Department of Meteorology, University of Reading, UK

14
15
16
17
18
19
20
21
22
23 **Corresponding author address:**

24 Room 1.2n, School of Geographical Sciences,

25 University Road, Bristol, BS8 1SS

26 United Kingdom

27
28 Email: c.j.r.williams@bristol.ac.uk

29
30 Short title: mid-Holocene and Last Interglacial experiments with HadGEM3

31 Keywords: Palaeoclimate, Quaternary change, mid-Holocene, Last Interglacial

32

33 **ABSTRACT**

34 Palaeoclimate model simulations are an important tool to improve our understanding of the
35 mechanisms of climate change. These simulations also provide tests of the ability of models to
36 simulate climates very different to today. Here we present the results from two brand-new
37 simulations using the latest version of the UK's physical climate model, HadGEM3-GC3.1; the mid-
38 Holocene (~6 ka) and Last Interglacial (~127 ka) simulations, both conducted under the auspices of
39 CMIP6/PMIP4. This is the first time this version of the UK model has been used to conduct
40 paleoclimate simulations. These periods are of particular interest to PMIP4 because they represent the
41 two most recent warm periods in Earth history, where atmospheric concentration of greenhouse gases
42 and continental configuration are similar to the pre-industrial period, but where there were significant
43 changes to the Earth's orbital configuration, resulting in a very different seasonal cycle of radiative
44 forcing.

45

46 Results for these simulations are assessed firstly against the same model's preindustrial control
47 simulation (a simulation comparison, to describe and understand the differences between the PI and
48 the two paleo simulations), and secondly against previous versions of the same model relative to
49 newly-available proxy data (a model-data comparison, to compare all available simulations from the
50 same model with proxy data to assess any improvements due to model advances). The introduction of
51 this newly available proxy data adds further novelty to this study. Globally, for metrics such as 1.5m
52 temperature and surface rainfall, whilst both the recent paleoclimate simulations are mostly capturing
53 the expected sign and, in some places, magnitude of change relative to the preindustrial, this is
54 geographically and seasonally dependent. Compared to newly-available proxy data (including SST
55 and rainfall), and also incorporating data from previous versions of the model, shows that the relative
56 accuracy of the simulations appears to vary according to metric, proxy reconstruction used for
57 comparison and geographical location. In some instances, such as mean rainfall in the mid-Holocene,
58 there is a clear and linear improvement, relative to proxy data, from the oldest to the newest
59 generation of the model. When zooming into northern Africa, a region known to be problematic for
60 models in terms of rainfall enhancement, the behaviour of the West African monsoon in both recent
61 paleoclimate simulations is consistent with current understanding, suggesting a wetter monsoon
62 during the mid-Holocene and (more so) the Last Interglacial, relative to the preindustrial era.
63 However, regarding the well-documented 'Saharan greening' during the mid-Holocene, results here
64 suggest that the most recent version of the UK's physical model is still unable to reproduce the
65 increases suggested by proxy data, consistent with all other previous models to date.

66

67

68 1. INTRODUCTION

69 Simulating past climates has been instrumental in improving our understanding of the mechanisms of
70 climate change (e.g. Gates 1976, Haywood *et al.* 2016, Jungclaus *et al.* 2017, Kageyama *et al.* 2017,
71 Kageyama *et al.* 2018, Kohfeld *et al.* 2013, Lunt *et al.* 2008, Otto-Bliesner *et al.* 2017, Ramstein *et al.*
72 1997), as well as in identifying and assessing discrepancies in palaeoclimate reconstructions (e.g.
73 Rind & Peteet 1985). Palaeoclimate scenarios can also provide tests of the ability of models to
74 simulate climates that are very different to today, often termed ‘out-of-sample’ tests. This notion
75 underpins the idea that robust simulations of past climates improve our confidence in future climate
76 change projections (Braconnot *et al.* 2011, Harrison *et al.* 2014, Taylor *et al.* 2011). Palaeoclimate
77 scenarios have also been used to provide additional tuning targets for models (e.g. Gregoire *et al.*
78 2011), in combination with historical or pre-industrial conditions.

79

80 The international Climate Model Intercomparison Project (CMIP) and the Palaeoclimate Model
81 Intercomparison Project (PMIP) have spearheaded the coordination of the international palaeoclimate
82 modelling community to run key scenarios with multiple models, perform data syntheses, and
83 undertake model-data comparisons since their initiation twenty-five years ago (Joussaume & Taylor
84 1995). Now in its fourth incarnation, PMIP4 (part of the sixth phase of CMIP, CMIP6), it includes a
85 larger set of models than previously, and more palaeoclimate scenarios and experiments covering the
86 Quaternary (documented in Jungclaus *et al.* 2017, Kageyama *et al.* 2017, Kageyama *et al.* 2018 and
87 Otto-Bliesner *et al.* 2017) and Pliocene (documented in Haywood *et al.* 2016).

88

89 PMIP4 specifies experiment set-ups for two interglacial simulations: the mid-Holocene (MH) at ~6 ka
90 and the Last Interglacial (LIG) at ~127 ka (although spanning ~129-116 ka in its entirety). These are
91 the two most recent warm periods (particularly in the Northern Hemisphere) in Earth history, and are
92 of particular interest to PMIP4; indeed, the MH experiment is one of the two entry cards into PMIP
93 (Otto-Bliesner *et al.* 2017). This is because whilst the atmospheric concentration of greenhouse gases,
94 the extent of land ice, and the continental configuration is similar in these PMIP4 set-ups compared to
95 the pre-industrial (PI) period, significant changes to the seasonal cycle of radiative forcing, relative to
96 today, do occur during these periods due to long-term variations in the Earth’s orbital configuration.
97 The MH and LIG both have higher boreal summer insolation and lower boreal winter insolation
98 compared to the PI, as shown by Figure 1, leading to an enhanced seasonal cycle in insolation as well
99 as a change in its latitudinal distribution. The change is more significant in the LIG than the MH, due
100 to the larger eccentricity of the Earth’s orbit at that time. Note that, in this figure and indeed all
101 subsequent figures using monthly or seasonal data, the data have been calendar adjusted (Joussaume
102 & Braconnot 1997) according to the method of Pollard & Reusch (2002) and Marzocchi *et al.* (2015);
103 see the Supplementary Material (SM1) for the same figure but using the modern calendar.

104

105 Palaeodata syntheses indicate globally warmer surface conditions of potentially $\sim 0.7^{\circ}\text{C}$ than PI in the
106 MH (Marcott *et al.* 2013) and up to $\sim 1.3^{\circ}\text{C}$ in the LIG (Fischer *et al.* 2018). During both warm
107 periods there is abundant palaeodata evidence indicating enhancement of Northern Hemisphere
108 summer monsoons (e.g. Wang *et al.* 2008) and in the case of the Sahara, replacement of desert by
109 shrubs and steppe vegetation (e.g. Drake *et al.* 2011, Hoelzmann *et al.* 1998), grassland and
110 xerophytic woodland/scrubland (e.g. Jolly *et al.* 1998a, Jolly *et al.* 1998b, Joussaume *et al.* 1999) and
111 inland water bodies (e.g. Drake *et al.* 2011, Lezine *et al.* 2011). Recent palaeodata compilations
112 involving either air temperatures or SST (Capron *et al.* 2014, Hoffman *et al.* 2017) reveal that the
113 maximum temperatures were reached asynchronously in the LIG between the Northern and Southern
114 Hemispheres. Concerning precipitation, historically this has been lacking relative to temperature or
115 SST reconstructions. One often-cited study for the MH is that of Bartlein *et al.* (2011), comprising a
116 combination of existing quantitative reconstructions based on pollen and plant macrofossils; this
117 provides evidence of the interaction between orbital variations and greenhouse gas forcing, and the
118 atmospheric circulation response. More recently, one newly-published dataset of LIG precipitation
119 proxy data (which the current study benefits from as part of the model-data comparison, see below) is
120 that of Scussolini *et al.* (2019). Here, a number of climate models are assessed against this brand-new
121 dataset, finding an agreement with proxy data over Northern Hemisphere landmasses, but less so in
122 the Southern Hemisphere (Scussolini *et al.* 2019).

123

124 Many modelling studies have been undertaken in an attempt to reproduce the changes suggested by
125 proxy data throughout the Quaternary, and especially during the interglacial periods discussed here,
126 and there is not scope in this current study to give a full review here. An overview of multi-model
127 assessments during the LIG can be found in Lunt *et al.* (2013). However, one example is the
128 aforementioned monsoon enhancement (and expansion/contraction) during the Quaternary, and
129 previous studies have focused on various aspects of this, such as whether any expansion was
130 hemispherically consistent or asynchronous between hemispheres (e.g. Kutzbach *et al.* 2008, McGee
131 *et al.* 2014, Singarayer & Burrough 2015, Singarayer *et al.* 2017, Wang *et al.* 2006, Wang *et al.*
132 2014). During the LIG, the aforementioned asynchronous temperature distribution between the
133 hemispheres has been investigated by a number of model simulations, suggesting that this may have
134 been caused by meltwater induced shutdown of the Atlantic Meridional Overturning Circulation
135 (AMOC) in the early part of the LIG, due to the melting of the Northern Hemisphere ice sheets during
136 the preceding deglaciation (e.g. Carlson 2008, Smith & Gregory 2009, Stone *et al.* 2016).

137

138 The driving mechanism producing the climate and environmental changes indicated by the palaeodata
139 for the MH and LIG is different to current and future anthropogenic warming, as the former results
140 from orbital forcing changes whilst the latter results from increases in greenhouse gases. Moreover,

141 the orbital forcing primarily acts on shortwave radiation whereas greenhouse gas changes primarily
142 act upon the longwave radiation flux, and the orbital forcing can lead to uneven horizontal and
143 seasonal changes whereas greenhouse gas forcing can cause more uniform anomalies (it should be
144 noted that whilst a precise calculation of the radiative forcing due to changes in MH and LIG
145 greenhouse gases is beyond the scope of this study, such a calculation could follow the methodology
146 of Gunnar *et al.* [1998]). Nevertheless, despite these differences in driving mechanism, these past
147 high latitude (and mainly Northern Hemisphere) warm intervals are a unique opportunity to
148 understand the magnitudes of forcings and feedbacks in the climate system that produce warm
149 interglacial conditions, which can help us understand and constrain future climate projections (e.g.
150 Holloway *et al.* 2016, Rachmayani *et al.* 2017, Schmidt *et al.* 2014). Running the same model
151 scenarios with ever newer models enables the testing of whether model developments are producing
152 improvements in palaeo model-data comparisons, assuming appropriate boundary conditions are used.
153 Previous iterations of PMIP, with older versions of the PMIP4 models, have uncovered persistent
154 shortcomings (Harrison *et al.* 2015) that have not been eliminated despite developments in resolution,
155 model physics, and addition of further Earth system components. One key example of this is the
156 continued underestimation of the increase in rainfall over the Sahara in the MH PMIP simulations
157 (e.g. Braconnot *et al.* 2012).

158

159 In this study we run and assess the latest version of the UK's physical climate model, HadGEM3-
160 GC3.1. Whilst older versions of the UK model have been included in previous iterations of CMIP,
161 and whilst present-day and future simulations from this model are included in CMIP6, the novelty of
162 this study is that this is the first time this version has been used to conduct any paleoclimate
163 simulations. In Global Coupled (GC) version 3 (and therefore in the following GC3.1), there have
164 been many updates and improvements, relative to its predecessors, which are discussed extensively in
165 Williams *et al.* (2017) and a number of companion scientific model development papers (see Section
166 2.1). As a brief introduction, however, GC3 includes a new aerosol scheme, multilayer snow scheme,
167 multilayer sea ice and several other parametrization changes, including a set relating to cloud and
168 radiation, as well as a revision to the numerics of atmospheric convection (Williams *et al.* 2017). In
169 addition, the ocean component of GC3 has other changes including an updated ocean and sea ice
170 model, a new cloud scheme, and further revisions to all parametrization schemes (Williams *et al.*
171 2017). See Section 2.1 for further details.

172

173 Following the CMIP6/PMIP4 protocol, here the PMIP4 MH and LIG simulations have been
174 conducted and assessed, with the assessment adopting a two-pronged approach. Firstly a simulation
175 comparison is made between these simulations and the same model's PI simulation (to describe and
176 understand the differences between them). Secondly a model-data comparison is made between the
177 current and previous versions of the same model relative to newly-available proxy data, thereby

178 assessing any improvements due to model advances. In addition to a global assessment, a secondary
179 focus of this paper is on the fidelity of the temperature anomalies and the degree of precipitation
180 enhancement in the Sahara, the latter of which has proved problematic for several generations of
181 models. Following this introduction, Section 2 describes the model, the experimental design, the
182 proxy data used for the model-data comparisons, and a brief discussion of the simulation spin-up
183 phases. Section 3 then presents the results, beginning with the simulation comparison and following
184 with the model-data comparison, and finally section 4 summarises and concludes.

185

186 **2. MODEL, EXPERIMENT DESIGN, DATA AND SPIN-UP SIMULATIONS**

187 **2.1. Model**

188 **2.1.1. Model terminology**

189 In this paper, and consistent with CMIP nomenclature, the ‘spin-up phase’ of the simulations refers to
190 when they are spinning up to atmospheric and oceanic equilibrium, whereas the ‘production run’
191 refers to the end parts (usually the last 50 or 100 years) of the simulation used to calculate the
192 climatologies, presented as the results. When discussed as geological intervals, the preindustrial, mid-
193 Holocene and Last Interglacial are referred to as the PI, MH and LIG respectively. In contrast, when
194 discussed as the three most recent simulations using HadGEM3 (see below), consistent with CMIP
195 they are referred to as the *piControl*, *midHolocene* and *lig127k* simulations, respectively. When the
196 *midHolocene* and *lig127k* are discussed collectively, they are referred to as the ‘warm climate
197 simulations’; whilst it is acknowledged that other factors differentiate these simulations such as orbital
198 configuration or CO₂, ‘warm climate simulations’ was deemed an appropriate collective noun.

199

200 **2.1.2. Model details**

201 The warm climate simulations conducted here, and the *piControl* simulation (conducted elsewhere as
202 part of the UK’s CMIP6 runs and used here for comparative purposes) were all run using the same
203 fully-coupled GCM: the Global Coupled 3 configuration of the UK’s physical climate model,
204 HadGEM3-GC3.1. Full details on HadGEM3-GC3.1, and a comparison to previous configurations,
205 are given in Williams *et al.* (2017) and Kuhlbrodt *et al.* (2018). Here, the model was run using the
206 Unified Model (UM), version 10.7, and including the following components: i) Global Atmosphere
207 (GA) version 7.1, with an N96 atmospheric spatial resolution (approximately 1.875° longitude by
208 1.25° latitude) and 85 vertical levels; ii) the NEMO ocean component, version 3.6, including Global
209 Ocean (GO) version 6.0 (ORCA1), with an isotropic Mercator grid which, despite varying in both
210 meridional and zonal directions, has an approximate spatial resolution of 1° by 1° and 75 vertical
211 levels; iii) the Global Sea Ice (GIS) component, version 8.0 (GSI8.0); iv) the Global Land (GL)
212 configuration, version 7.0, of the Joint UK Land Environment Simulator (JULES); and v) the OASIS3
213 MCT coupler. The official title for this configuration of HadGEM3-GC3.1 is HadGEM3-GC31-LL
214 N96ORCA1 UM10.7 NEMO3.6 (for brevity, hereafter HadGEM3).

215
216 All of the above individual components are summarised by Williams *et al.* (2017) and detailed
217 individually by a suite of companion papers (see Walters *et al.* 2017 for GA7 and GL7, Storkey *et al.*
218 2017 for GO6 and Ridley *et al.* 2017 for GIS8). However, a brief description of the major changes
219 relative to its predecessor are given in the Supplementary Material. When all of these components are
220 coupled together to give GC3, there have been several improvements relative to its predecessor
221 (GC2), most noticeably to the large warm bias in the Southern Ocean (which was reduced by 75%), as
222 well as an improved simulation of clouds, sea ice, the frequency of tropical cyclones in the Northern
223 Hemisphere as well as the AMOC, and the Madden Julian Oscillation (MJO) (Williams *et al.* 2017).
224 Relative to the previous fully-coupled version of the model (HadGEM2), which was submitted to the
225 last CMIP5/PMIP3 exercise, many systematic errors have been improved including a reduction of the
226 temperature bias in many regions, a better simulation of mid-latitude synoptic variability, and an
227 improved simulation of tropical cyclones and the El Niño Southern Oscillation (ENSO) (Williams *et*
228 *al.* 2017).

229
230 Here, the *midHolocene* and *lig127k* simulations were both run on the UK National Supercomputing
231 Service, ARCHER, whereas the *piControl* was run on a different platform based within the UK Met
232 Office's Hadley Centre. While this may mean that anomalies computed against the *piControl* are
233 potentially influenced by different computing environments, and not purely the result of different
234 climate forcings, the reproducibility of GC3.1 simulations across different platforms has been tested
235 (Guarino *et al.* 2020a). It was found that, although a simulation length of 200 years is recommended
236 whenever possible to adequately capture climate variability across different platforms, the main
237 climate variables considered here (e.g. surface temperature) are not expected to be significantly
238 different on a 100- or 50-year timescale (see, for example, Fig. 6 in Guarino *et al.* [2020a]) as they are
239 not directly affected by medium-frequency climate processes.

240 241 **2.2. Experiment design**

242 Full details of the experimental design and results from the CMIP6 *piControl* simulation are
243 documented in Menary *et al.* (2018). Both the warm climate simulations followed the experimental
244 design given by Otto-Bliesner *et al.* (2017), and specified at
245 https://pmip4.lsce.ipsl.fr/doku.php/exp_design:index. The primary differences from the *piControl*
246 were to the astronomical parameters and the atmospheric trace greenhouse gas concentrations,
247 summarised in Table 1. For the astronomical parameters, these were prescribed in Otto-Bliesner *et al.*
248 (2017) according to orbital constants from Berger & Loutre (1991). However, in HadGEM3, the
249 individual parameters (e.g. eccentricity, obliquity, etc) use orbital constants based on Berger (1978),
250 according to the specified start date of the simulation. For the atmospheric trace greenhouse gas

251 concentrations, these were based on recent reconstructions from a number of sources (see Table 1 for
252 values, and section 2.2 in Otto-Bliesner *et al.* [2017] for a full list of references/sources).

253

254 All other boundary conditions, including solar activity, ice sheets, topography and coastlines, volcanic
255 activity and aerosol emissions, are identical to the CMIP6 *piControl* simulation. Likewise, vegetation
256 was prescribed to present-day values, to again match the CMIP6 *piControl* simulation. As such, the
257 *piControl* and both the warm climate simulations actually include a prescribed fraction of urban land
258 surface. As a result of this, our orbitally- and greenhouse gas-forced simulations should be considered
259 as anomalies to the *piControl*, rather than absolute representations of the MH or LIG climate.

260

261 Both the warm climate simulations were started from the end of the *piControl* spin-up phase (which
262 ran for approximately 600 years), after which time the *piControl* was considered to be in atmospheric
263 and oceanic equilibrium (Menary *et al.* 2018). To assess this, four metrics were used, namely net
264 radiative balance at the top of the atmosphere (TOA), surface air temperature (SAT), full-depth ocean
265 temperature (OceTemp) and full-depth ocean salinity (OceSal) (Menary *et al.* 2018). See Section 2.4
266 (and in particular Table 2) for an analysis of the equilibrium state of both the *piControl* and the warm
267 climate simulations. Starting at the end of the *piControl*, these were then run for their own spin-up
268 phases, 400 and 350 years for the *midHolocene* and *lig127k* respectively. Once the simulations were
269 considered in an acceptable level of equilibrium (see Section 2.4), a production phase was run for 100
270 and 200 years for the *midHolocene* and *lig127k* respectively, during which the full CMIP6/PMIP4
271 diagnostic profile was implemented to output both high and low temporal frequency variables.

272

273 **2.3. Data**

274 Recent data syntheses compiling quantitative surface temperature and rainfall reconstructions were
275 used in order to evaluate the warm climate simulations.

276

277 For the MH, the global-scale continental surface mean annual temperature (MAT) and rainfall (or
278 mean annual precipitation, MAP) reconstructions from Bartlein *et al.* (2011), with quantitative
279 uncertainties accounting for climate parameter reconstruction methods, were used (see Data
280 Availability for access details). They rely on a combination of existing quantitative reconstructions
281 based on pollen and plant macrofossils and are inferred using a variety of methods (see Bartlein *et al.*
282 2011 for further details). At each site, the 6 ka anomaly (corresponding to the 5.5-6.5 ka average
283 value), is given relative to the present day, and in the case where modern values could not be directly
284 inferred from the record, modern climatology values (1961-1990) were extracted from the Climate
285 Research Unit historical climatology data set (New *et al.* 2002). Further proxy data for the MH, such
286 as SST reconstructions, are not included here, as an extensive model-data comparison is presented in a
287 companion paper (Brierley *et al.* 2020).

288

289 For the LIG, two recent different sets of surface temperature data are available. Firstly, the Capron *et*
290 *al.* (2017) 127 ka timeslice of SAT and sea surface temperature (SST) anomalies (relative to pre-
291 industrial, 1870-1899), is based on polar ice cores and marine sediment data that are (i) located
292 poleward of 40° latitude and (ii) have been placed on a common temporal framework (see Data
293 Availability for access details). Polar ice core water isotope data are interpreted as annual mean
294 surface air temperatures, while most marine sediment-based reconstructions are interpreted as summer
295 (defined here as July-September, JAS) SST signals. For each site, the 127 ka value was calculated as
296 the average value between 126 and 128 ka using the surface temperature curve resampled every 0.1
297 ka. Here, we use the SST anomalies only. Secondly, a global-scale time slice of SST anomalies,
298 relative to pre-industrial (1870-1889), at 127 ka was built, based on the recent compilation from
299 Hoffman *et al.* (2017), which includes both annual and summer SST reconstructions (see Data
300 Availability for access details). This adds further novelty to this study, by using a new combined
301 dataset based on this existing data. The 127 ka values at each site were extracted, following the
302 methodology they proposed for inferring their 129, 125 and 120 ka time slices i.e. the SST value at
303 127 ka was taken on the provided mean 0.1 ka interpolated SST curve for each core location. Data
304 syntheses from both Capron *et al.* (2014, 2017) and Hoffman *et al.* (2017) are associated with
305 quantitative uncertainties accounting for relative dating and surface temperature reconstruction
306 methods. Here, the two datasets are treated as independent data benchmarks, as they use different
307 reference chronologies and methodologies to infer temporal surface temperature changes, and
308 therefore they should not be combined. See Capron *et al.* (2017) for a detailed comparison of the two
309 syntheses. A model-data comparison exercise using existing LIG data compilations focusing on
310 continental surface temperature (e.g. Turney and Jones 2010) was not attempted, as they do no benefit
311 yet from a coherent chronological framework, preventing the definition of a robust time slice
312 representing the 127 ka terrestrial climate conditions (Capron *et al.* 2017).

313

314 A brand-new, recently-published dataset of proxy precipitation anomalies (again, relative to the
315 preindustrial) is also used for model-data comparison purposes here, adding further novelty to this
316 study. The proxy data are compiled from existing literature by Scusscolini *et al.* (2019), and the
317 dataset includes 138 proxy locations from a number of paleoclimatic archives including pollen, fossils
318 other than pollen, lacustrine or marine sediment composition, loess deposits, and other multi-proxy
319 sources. Note that, as Scusscolini *et al.* (2019) observe, unlike temperature anomalies the majority of
320 precipitation anomalies in the existing literature are not quantitative. To allow a quantitative
321 comparison, Scusscolini *et al.* (2019) use a semi-quantitative scale, based on their expert judgement,
322 to show a LIG that is ‘much wetter’, ‘wetter’, ‘no discernible change’, ‘drier’ and ‘much drier’,
323 relative to the PI. The same scale is therefore used here. See Scusscolini *et al.* (2019) for further
324 information, and see Data Availability for access details).

325

326 **2.4. Spin-up simulations**

327 As briefly mentioned above, both the warm climate simulations had a spin-up phase before the main
328 production run was started, briefly discussed here. As an example of atmospheric equilibrium, annual
329 global mean 1.5 m air temperature and TOA radiation from both warm climate simulations, compared
330 to the *piControl*, are summarised in Table 2; see Supplementary Material (SM2) for the timeseries of
331 these fields. For the warm climate simulations, despite considerable interannual variability and
332 arguably more so than in the *piControl* (see SM2), both are showing long-term trends of -0.06°C
333 century^{-1} and $-0.16^{\circ}\text{C century}^{-1}$ for the last 100 years of the *midHolocene* and *lig127k*, respectively
334 (Table 2). The spatial patterns of these trends, also shown in the Supplementary Material (SM3), are
335 similar in both warm climate simulations, with much of the statistically significant cooling occurring
336 over high latitude regions in both Hemispheres, and particularly so over Antarctica in the *lig127k*
337 simulation (SM3). The TOA radiation balance is also showing long-term (and again slightly
338 negative) trends by the end of the simulations, with -0.05 W m^2 and -0.06 W m^2 for the the
339 *midHolocene* and *lig127k*, respectively.

340

341 As an example of oceanic equilibrium, annual global mean full-depth OceTemp and OceSal are
342 shown in Table 2 (and again visualised in the Supplementary Material, SM4). OceTemp is steadily
343 increasing throughout the *piControl*, and this continues in both warm climate simulations, whereas
344 there is a dramatic fall in ocean salinity in these simulations (SM4). Concerning the long-term trends,
345 Menary *et al.* (2018) considered values acceptable for equilibrium to be $< +/-0.035^{\circ}\text{C century}^{-1}$ and $<$
346 $+/-0.0001 \text{ psu century}^{-1}$ (for OceTemp and OceSal, respectively); as shown in Table 2, although both
347 warm climate simulations meet the temperature criterion, the *midHolocene* it is not meeting the
348 salinity criterion (-0.0004 psu). However, running for several thousands of years (and > 5 years of
349 computer time), which would be needed to reach true oceanic equilibrium, was simply unfeasible here
350 given time and resource constraints.

351

352 **3. RESULTS**

353 **3.1. Production runs results**

354 The warm climate production runs were undertaken following the spin-up phase, with the climatology
355 of each simulation being compared to that from the *piControl*, as well as available proxy data, using
356 either annual means or summer/winter seasonal means. For the latter, depending on the availability of
357 the proxy data, Northern Hemisphere summer is defined as either June-August (JJA) or JAS, and
358 Northern Hemisphere winter is defined as either December-February (DJF) or January-March (JFM);
359 and vice versa for Southern Hemisphere summer/winter. As briefly introduced in Section 1, the focus
360 is on two separate measures: i) to describe and understand the differences between the two most

361 recent warm climate simulations and the *piControl* in terms of temperature, rainfall and
362 atmospheric/oceanic circulation changes; and ii) to compare both current simulations, as well as
363 simulations from previous versions of the UK model (where available), with the aforementioned
364 newly-available proxy data, to assess any improvements due to model advances. A final aim,
365 discussed only briefly here but shown in the Supplementary Material, is to include previous CMIP5
366 models to address the question of whether any of the simulations produce enough rainfall to allow
367 vegetation growth across the Sahara: the mid-Holocene ‘Saharan greening’.

368

369 **3.1.1. Do the CMIP6 HadGEM3 warm climate simulations show temperature, rainfall and** 370 **atmospheric/oceanic circulation differences when compared to the pre-industrial era?**

371 Here we focus on mean differences between the HadGEM3 warm climate simulations and the
372 corresponding *piControl*. Calendar adjusted annual and seasonal mean summer/winter 1.5 m air
373 temperature anomalies (relative to the *piControl*) from both warm climate simulations are shown in
374 Figure 2. As an example and for comparative purposes, the same figure but where the data are based
375 on the modern calendar is shown in the Supplementary Material (SM5); this suggests that the impact
376 of the calendar adjustments on this field, and at this spatial and temporal scale, is negligible, with the
377 only obvious impact occurring over the Northern Hemisphere polar regions during JJA in both
378 simulations, but more so in the *lig127k* simulation (due to the larger changes in insolation resulting in
379 a larger change to the calendar, relative to the MH). Consistent with the seasonality of the changes,
380 the differences between either simulation are less at the annual timescale (Figure 2a and d) than
381 during individual seasons, but are still nevertheless statistically significant at the 99% level. During
382 JJA, the *midHolocene* is showing a widespread statistically significant increase in temperatures of up
383 to 2°C across the entire Northern Hemisphere north of 30°N, more in some places e.g. Greenland
384 (Figure 2b), consistent with the increased latitudinal and seasonal distribution of insolation caused by
385 known differences in the Earth’s axial tilt (Berger & Loutre 1991, Otto-Bliesner *et al.* 2017). The
386 only places showing a reduction in temperature are West and Central Africa (around 10°N) and
387 northern India; this, as discussed below, is likely related to increased rainfall in response to a stronger
388 summer monsoon, but could also be due to the resulting increase in cloud cover (reflecting more
389 insolation) or a combination of the two. During DJF, only the Northern Hemisphere high latitudes
390 (north of 60°N) continue this warming trend, with the rest of continental Africa and Asia showing a
391 reduction in temperature (Figure 2c). These patterns are virtually the same in the *lig127k* simulation
392 (Figure 2e and f), just much more pronounced (with statistically significant temperature increases
393 during JJA of 5°C or more); again, this is consistent with the differences in the Earth’s axial tilt, which
394 were more extreme (and therefore Northern Hemisphere summer experienced larger insolation
395 changes) in the LIG relative to the MH (Berger & Loutre 1991, Otto-Bliesner *et al.* 2017). Another
396 clear feature of these figures, at either annual or seasonal timescales, is polar amplification, which is
397 likely associated with changes in sea-ice; as shown in the Supplementary Material (SM6), statistically

398 significant decreases in sea-ice are shown throughout the polar regions of both hemispheres in the
399 *midHolocene*, relative to the *piControl*. The same is true for the *lig127k* simulation, just more
400 pronounced (not shown).

401

402 Calendar adjusted seasonal mean summer and winter surface daily rainfall anomalies (again relative
403 to the *piControl*) from both warm climate simulations are shown in Figure 3. In line with the
404 aforementioned increased latitudinal and seasonal distribution of insolation, the largest differences in
405 either simulation occur during Northern Hemisphere summer (Figure 3b and e). Both warm climate
406 simulations are showing statistically against increases in rainfall around the monsoon regions,
407 especially over northern India and equatorial Africa, more so in the *lig127k* (Figure 3e). Both
408 simulations are also showing oceanic drying relative to the *piControl*, especially in the equatorial
409 Atlantic and Pacific, again more pronounced in the *lig127k* (Figure 3e). In contrast, during DJF, less
410 of an impact is seen in either simulation relative to the *piControl*, with a small but statistically
411 significant increase in rainfall in oceanic equatorial regions but drying over tropical land regions e.g.
412 southern Africa, central Brazil and northern Australia (Figure 3c and f). Again, consistent with the
413 increased insolation changes during the LIG compared to the MH, these differences are stronger in the
414 *lig127k* simulation (Figure 3f). Consistent with the temperature differences, these signals are again
415 weaker at the annual timescale but are nevertheless statistically significant (Figure 3a and b).

416

417 A measure of oceanic circulation is also considered here, shown by the three HadGEM3 simulations
418 of meridional overturning circulation (MOC) in the Atlantic basin and globally (Figure 4a-c and d-f,
419 respectively). Although not identical, the differences are nevertheless negligible, with both warm
420 climate simulations almost exactly reproducing the structures of weakly and strongly overturning
421 MOC seen in the *piControl*; for example, the strongly overturning MOC in the upper levels of the
422 Atlantic is marginally stronger in the *midHolocene* at ~30-40°N relative to the other two simulations,
423 but the structures are very similar. This suggests that the changes to atmospheric fields such as P-E,
424 energy fluxes and wind stress (in response to the insolation changes) are having a minimal impact on
425 the overturning circulation, and this is consistent with other work (e.g. Guarino *et al.* [2020b]).

426

427 A key region of interest, concerning mean precipitation changes and changes to the extent and
428 latitudinal distribution of monsoon regions, is northern Africa, primarily because of the
429 aforementioned inability of previous models to reproduce the increases shown by the proxy data here
430 (e.g. Braconnot *et al.* 2007, Braconnot *et al.* 2012). Therefore, Figure 5 reproduces the above
431 precipitation changes but zooms into Africa and additionally includes calendar adjusted mean JJA (the
432 primary monsoon region) 850mb wind anomalies (relative to the *piControl*). In response to the
433 increased Northern Hemisphere summer insolation, the West African monsoon is enhanced in both
434 simulations, with positive (negative) rainfall anomalies across sub-Saharan Africa (eastern equatorial

435 Atlantic) suggesting a northward displacement of the rainfall maxima. This is consistent with
436 previous work, with a northward movement of the rainbelt being associated with increased advection
437 of moisture into the continent (Huag *et al.* 2001, Singarayer *et al.* 2017, Wang *et al.* 2014). This
438 increased advection of moisture is shown by the enhanced low-level westerlies at all latitudes but
439 especially over the regions of rainfall maxima in Figure 5a and b, drawing in more moisture from the
440 tropical Atlantic, which are consistent with previous work documenting the intensified monsoon
441 circulation (Huag *et al.* 2001, Singarayer *et al.* 2017, Wang *et al.* 2006). This pattern is enhanced in
442 the *lig127k* relative to the *midHolocene*, again in response to the stronger insolation changes relative
443 to the MH, and the northward displacement of the central rainbelt is more pronounced in the *lig127k*
444 simulation (Figure 5c).

445

446 The change to the intensity and the spatial pattern (e.g. latitudinal positioning and extent) of the West
447 African monsoon is further shown in Figure 6, which shows calendar adjusted daily JJA rainfall by
448 latitude over West Africa (averaged over 20°W-15°E, land points only) from both warm climate
449 simulations. This figure also includes MH and LIG simulations from previous generations of the
450 same model. It should be noted that although LIG experiments have been conducted previously with
451 both model-model and model-data comparisons being made (Lunt *et al.* 2013), all of these
452 experiments were carried out using early versions of the models and were thus not included in
453 CMIP5. Moreover, as part of their assessment Lunt *et al.* (2013) considered a set of four simulations,
454 at 130, 128, 125 and 115 ka, none of which are directly comparable to the current HadGEM3 *lig127k*
455 simulation. Instead, a LIG simulation has recently been undertaken using one of the original versions
456 of the UK's physical climate model, HadCM3, and so this is used here to compare with the *lig127k*
457 simulation.

458

459 Beginning with the recent paleoclimate HadGEM3 simulations, in line with the changes in insolation
460 both warm climate simulations are showing higher absolute values at their peak (between ~7.5-10°N)
461 than the *piControl* (Figure 6a). Concerning anomalies, both simulations are showing a large increase
462 in rainfall relative to the *piControl* (of ~2 and 6 mm day⁻¹ for the *midHolocene* and *lig127k*,
463 respectively) over the monsoon region between ~10-12°N (Figure 6b). Relative to previous versions
464 of the same model, the previous generation (HadGEM2-ES) is slightly drier than HadGEM3 over this
465 region for its PI simulation and slightly wetter for its MH simulation; conversely, the version before
466 that (HadCM3) is consistently wetter than HadGEM3, for all of its simulations (Figure 6a). There
467 also appears to be a northward displacement in the oldest version, with the largest difference between
468 the simulations and their corresponding PI simulations occurring at ~11°N in the two most recent
469 versions of the model, whereas in HadCM3 this appears to be shifted northwards to ~12.5°N (Figure
470 6b). This northward displacement in certain models is consistent with previous work (e.g. Huag *et al.*
471 2001, Otto-Bliesner *et al.* 2017, Singarayer *et al.* 2017, Wang *et al.* 2014). In terms of the latitudinal

472 extent, the results suggest that all warm climate simulations (regardless of generation) are producing a
473 wider Northern Hemisphere monsoon region (i.e. a greater northerly extent) relative to each version's
474 PI, with rainfall falling to near zero at ~18°N in the PI simulations but extending to 20°N (and above,
475 in terms of the LIG simulations) in both warm climate simulations (Figure 6a). This is again
476 consistent with previous work, where various theories are compared as to the reasons behind the
477 latitudinal changes in the rainbelt's position, one which is a symmetric expansion during boreal
478 summer (Singarayer & Burrough 2015, Singarayer et al. 2017).

479

480 **3.1.2. Simulation comparison and Model-Data comparison: Do the CMIP6 HadGEM3** 481 **simulations reproduce the 'reconstructed' climate based on available proxy data, and has there** 482 **been any noticeable improvement relative to previous versions of the same model?**

483 Although the above analysis is useful and confirms that the most recent warm climate simulations are
484 responding consistently to the increased latitudinal and seasonal distribution of insolation, it does not
485 give any information on which (if any) of the simulations is most accurate or which version of the
486 model is better at reproducing proxy-observed conditions. Therefore, here we bring in a comparison
487 with newly-available proxy data, comparing these to all versions of the model, focusing on surface air
488 temperature, SST and rainfall (drawing direct comparisons, as well as using the root mean square
489 error (RMSE, but without a cut-off threshold), between both proxy vs simulated data and HadGEM3
490 vs previous versions. The aim of this is to firstly see how well the current warm climate simulations
491 are reproducing the 'observed' approximate magnitudes and patterns of change, and secondly to
492 assess any possible improvement from previous versions of the same model. It is worth noting that
493 both simulated and proxy anomalies contain a high level of uncertainty (as measured by the standard
494 deviation), and in many locations the uncertainty is larger than the anomalies themselves (not shown).
495 The following results should therefore be considered with this caveat in mind.

496

497 Before the spatial patterns are compared, it is useful to assess global means from the three HadGEM3
498 simulations (focusing on 1.5 m air temperature, calculated both annually and during Northern and
499 Southern Hemisphere summer, JJA and DJF respectively). Table 3 shows these global means, where
500 it is clear that when annual means are considered, the *midHolocene* simulation is actually cooler than
501 the *piControl*. This discrepancy with the palaeodata, which at many locations suggests a warmer MH
502 relative to PI, is consistent with previous work using other models (e.g. Lui *et al.* 2014). The *lig127k*
503 simulation is, however, warmer than the *piControl* simulation. Given the seasonal distribution of
504 insolation in these two simulations, it is expected that the largest difference to the *piControl* occurs
505 during boreal summer, and indeed it does; during JJA, there is a warmer *lig127k* and a slightly
506 warmer *midHolocene* (1.69°C and 0.07°C, respectively). The opposite is true during DJF.

507

508 Concerning the spatial patterns during the MH, Figure 7 shows simulated surface MAT anomalies
509 from the current *midHolocene* simulation and those from two previous versions of the same model,
510 versus MH proxy anomalies from Bartlein *et al.* (2011). Note that, here, statistical significance of the
511 simulated anomalies has not been shown, because firstly the aim here is to assess all differences
512 regardless of significance and secondly because a measure of statistical significance (for HadGEM3)
513 has already been presented in Figure 2; statistical significance from the other versions of the same
514 model is virtually identical (not shown). Globally, all three models are showing a reasonable level of
515 agreement to the proxy data, with RMSE = 2.45°C, 2.42°C and 2.37°C for HadGEM3, HadGEM2-ES
516 and HadCM3, respectively (Table 4a). Using this metric, the oldest version of the model (HadCM3)
517 is doing marginally better than the other models, relative to the proxy data. Spatially, however, there
518 are differences to the proxy data and between model generations. Although all three generations
519 appear to be able to reproduce the sign of temperature change for many locations, with both simulated
520 and proxy anomalies suggesting increases in temperature North of 30°N and especially over northern
521 Europe, the Arctic Circle increases are not as homogenous in HadCM3 (Figure 7d) and indeed this
522 model shows cooling over the Greenland Sea. Although this cannot be corroborated by the proxy
523 data, due to a lack of coverage, neither of the later generation models show this to the same extent
524 (Figure 7b and c). Discrepancies with the proxy data also occur in all three simulations across the
525 Mediterranean region, where all three simulations suggest a small warming but the proxy data indicate
526 cooling (Figure 7). Moreover, regarding the magnitude of change, all three simulations are
527 underestimating the temperature increase across most of the Northern Hemisphere, with for example
528 increases of up to 1°C across Europe from the simulations compared to 3-4°C increases from the
529 proxy data. In the simulations, temperature anomalies only reach these magnitudes in the Northern
530 Hemisphere polar region (i.e. north of 70°N), not elsewhere. Further equatorward, all three
531 simulations are identifying a slight cooling over the West African monsoon region (as discussed
532 above), but the accuracy of this relative to the proxy data is difficult to ascertain given the lack of
533 coverage across Africa and, where there are data locations, a highly variable sign of change (Figure
534 7a).

535

536 A similar conclusion can be drawn from MAP, shown in Figure 8, where all three simulations are
537 correctly reproducing the sign of change across most of the Northern Hemisphere, although more so
538 in the two most recent generations of the model (HadGEM3 and HadGEM2-ES), but in some places
539 not the magnitude. Over the eastern US, for example, rainfall decreases of up to 200 mm yr⁻¹ are
540 being shown by the simulations (Figure 8b-d) whereas the proxy data suggests a much stronger drying
541 of up to 400 mm yr⁻¹ (Figure 8a). Elsewhere, such as over Europe and Northern Hemisphere Africa,
542 the simulations more accurately reproduce the magnitude of rainfall increases; both simulated and
543 proxy anomalies show increases of 200-400 mm yr⁻¹. Globally, Table 4a suggests that the most recent
544 generation model, HadGEM3, is doing better than the others, relative to the proxy data (RMSE =

545 285.9 mm yr⁻¹, 293.5 mm yr⁻¹ and 304.7 mm yr⁻¹ for HadGEM3, HadGEM2-ES and HadCM3,
546 respectively). In terms of how the spatial patterns change according to model version, during the MH
547 the two most recent simulations generally agree (RMSE = 90.8 mm year⁻¹, Table 4a) and show similar
548 spatial patterns; focusing again on the African monsoon region (for the aforementioned reasons), both
549 simulations show a drier equatorial Atlantic during the MH and then increased rainfall around 10°N
550 (Figure 8b and c for HadGEM3 and HadGEM2-ES, respectively). Both simulations also suggest that
551 the increases in rainfall extend longitudinally across the entire African continent, with the largest
552 changes not only occurring across western and central regions but also further east. In contrast,
553 globally HadCM3 agrees less with HadGEM3 (RMSE = 121.8 mm year⁻¹, Table 4a) and only
554 suggests a wetter MH over West Africa, not further east. HadCM3, and indeed HadGEM2-ES, also
555 differs from the most recent simulation over the equatorial Atlantic, showing a region of drying that is
556 not only stronger in magnitude but also larger in terms of spatial extent; whilst still present in
557 HadGEM3, this feature that is much weaker (Figure 8b-d).

558

559 Concerning the spatial patterns during the LIG, Figure 9 shows simulated mean SST anomalies
560 (calculated both annually and during JAS/JFM) from the current *lig127k* simulation and that from the
561 oldest version of the same model, versus LIG proxy anomalies from two sources, Capron *et al.* (2017)
562 and Hoffman *et al.* (2017). No LIG simulation using HadGEM2-ES is currently available. When
563 annual anomalies are considered, there is relatively good agreement globally between HadGEM3 and
564 the proxy data where RMSE = 3.03°C and 2.42°C for the Capron *et al.* (2017) and Hoffman *et al.*
565 (2017) data, respectively (Table 4b). HadCM3 performs marginally better when compared to the
566 Capron *et al.* (2017) data, but worse when compared to the Hoffman *et al.* (2017) data (Table 4b).
567 Similarly varying results also occur when JAS and JFM anomalies are considered, with HadGEM3
568 comparing slightly better or worse than HadCM3 according to season and proxy dataset used; all of
569 the values, however, show relatively good agreement, with no simulation exceeding RMSE = 4.5°C in
570 any season or with any dataset (Table 4b). Spatially, HadGEM3 is showing a general agreement
571 between simulated and proxy annual and JAS anomalies in the Northern Hemisphere (and in
572 particular in the North Atlantic), with both suggesting increased temperatures during the LIG of up to
573 5°C (Figure 9a and b). HadCM3 is not capturing these magnitudes at the annual timescale (Figure 9d)
574 and, despite showing greater warming during JAS, is still lower than HadGEM3; this is more in
575 agreement with the proxy data at higher latitudes (e.g. the western Norwegian Sea at ~70°N) but less
576 so further south (Figure 9e). This might suggest that, in this region, HadGEM3 is actually
577 overestimating the degree of warming. Nevertheless, in both versions of the model there are
578 discrepancies concerning not just in the magnitude but also in the sign of change, such as in the
579 eastern Norwegian Sea or the Labrador Sea, where reconstructions suggest a cooler LIG but both
580 versions show a consistent warming (Figure 9b and e). This is, however, consistent with previous
581 work, and earlier climate models have also failed to capture this cooling (Capron *et al.* 2014, Stone *et*

582 *al.* 2016). In Southern Hemisphere summer, JFM, both versions agree on a general (but weak)
583 cooling in the South Atlantic relative to preindustrial and a weak warming in the Southern Ocean
584 (Figure 9c and f). In contrast certain proxy locations (such as off the coast of southern Africa) suggest
585 a much warmer LIG than preindustrial, which is opposite to the simulated cooling in the same region
586 (Figure 9c and f). Further south, the majority of simulated anomalies reproduce the observed sign of
587 change, but not the magnitude; here, the simulations suggest temperature increases of up to 1°C,
588 whereas both proxy datasets suggest SST increases of 2-3°C depending on location (Figure 9c and f).

589

590 For rainfall changes during the LIG, Figure 10 shows simulated annual mean surface rainfall
591 anomalies from the current *lig127k* simulation and that from the oldest version of the same model,
592 versus LIG proxy anomalies from Scusscolini et al. (2019). Note that the simulated anomalies shown
593 here are annual anomalies, as opposed to daily anomalies in Figure 3, to be consistent with the proxy
594 data. Note also that, for these proxy reconstructions, a semi-quantitative scale is used by Scusscolini
595 et al. (2019) rather than actual anomalies and is therefore reproduced here; this ranges from a unitless
596 -2 to 2, corresponding to ‘Much wetter LIG anomaly’, ‘Wetter’, ‘No noticeable anomaly’, ‘Drier’ and
597 ‘Much drier LIG anomaly’. It is for this reason that RMSE values have not been calculated here. As
598 was suggested from the MH simulations (Figure 8), both versions of the model are showing similar
599 patterns of rainfall changes, along the same lines as those seen during the MH but again enhanced
600 (Figure 10). Both versions are showing enhanced rainfall across the Northern Hemisphere equatorial
601 zone and in particular the monsoon regions during the LIG, often exceeding 500 mm year⁻¹ in some
602 places. In the Northern Hemisphere, both versions of the model are generally in agreement with the
603 proxy data, with most proxy locations showing ‘Wetter’ or ‘Much wetter’ conditions. There are,
604 however, some discrepancies elsewhere, such as the regions of tropical drying over e.g. Brazil and
605 southern Africa in the simulations being in stark contrast to the ‘Wetter’ conditions suggested by the
606 proxy data (Figure 10). Concerning the differences in the spatial patterns between the model versions,
607 although both generations qualitatively show similar patterns, there are subtle differences. Again
608 focusing on the African monsoon region, HadGEM3 shows greatly increased rainfall across all of
609 sub-Saharan Africa, centred on 10°N but extending from ~5°N to almost 20°N and longitudinally
610 across the entire African continent (Figure 10a). In contrast, and similar to the MH results, in
611 HadCM3 the largest rainfall increases are less apparent over East Africa (Figure 10b).

612

613 It would therefore be reasonable to say that, for both MH and LIG simulations, whilst the most recent
614 version of the model is capturing the sign and magnitude of change relative to proxy reconstructions
615 (for either temperature or rainfall) in some locations, this is highly geographically dependent and there
616 are locations where the current simulation fails to capture even the sign of change. Compared to
617 previous versions of the same model, any improvement also appears to be highly variable according
618 to metric, proxy reconstruction used for comparison and geographical location, with for example

619 HadGEM3 showing some improvement relative to previous versions for rainfall during the MH, but
620 not surface air temperature. The accuracy of the most recent model, and indeed previous generations,
621 also appears to be seasonally dependent, with the most recent *lig127k* simulation correctly
622 reproducing both the sign and magnitude of change during Northern Hemisphere summer in some
623 locations, but not during Southern Hemisphere summer or annually. It would also appear that, for
624 both the MH and LIG simulations, whilst there is less difference between the most recent two
625 configurations of the model, they are nevertheless quite different to the oldest version. For global
626 mean annual rainfall during the MH, Table 4a shows a linear progression of improvement across the
627 three versions of the model, as well as more agreement between the two most recent model
628 generations. This is also true when just the region of rainfall maxima in northern Africa is considered,
629 with both of the two most recent generations, and especially HadGEM2-ES, being marginally closer
630 to the proxy data than HadCM3 (RMSE = 463.7 mm yr⁻¹, 424.5 mm yr⁻¹ and 468.4 mm yr⁻¹ for
631 HadGEM3, HadGEM2-ES and HadCM3, respectively). In all simulations, although spatial patterns
632 of rainfall are similar, there are discrepancies especially over the African monsoon region; the oldest
633 version of the model, for example, only shows rainfall increases over West Africa, whereas the two
634 most recent versions imply Africa-wide rainfall increases at this latitude. If a comparison is made
635 with satellite-derived rainfall data for the modern West African monsoon (not shown), results suggest
636 that rainfall maxima are not just limited to West Africa but also occur over the central region and East
637 Africa, more consistent with the two most recent versions of the model. One reason for HadCM3 not
638 identifying this longitudinal extent might be connected to the very coarse spatial resolution of this
639 model, relative to the others, impacting any topographically-induced rainfall, especially over the East
640 African Highlands.

641

642 **3.1.3. Saharan greening**

643 Finally, a brief discussion is given on the ‘Saharan greening’ question. Given that the warm climate
644 simulations, and indeed the *piControl*, did not use interactive vegetation, it is not possible to directly
645 test if the model is reproducing the Saharan greening that proxy data suggest. For example, Jolly *et*
646 *al.* (1998a, 1998b) analysed MH pollen assemblages across northern Africa and suggested that some
647 areas south of 23°N (characterised by desert today) were grassland and xerophytic
648 woodland/scrubland during the MH (Joussaume *et al.* 1999). To circumvent this caveat, Joussaume *et*
649 *al.* (1999) developed a method for indirectly assessing Saharan greening, based on the annual mean
650 rainfall anomaly relative to a given model’s modern simulation. Using the water-balance module
651 from the BIOME3 equilibrium vegetation model (Haxeltine & Prentice 1996), Joussaume *et al.*
652 (1999) calculated the increase in mean annual rainfall, zonally averaged over 20°W-30°E, required to
653 support grassland at each latitude from 0 to 30°N, compared to the modern rainfall at that latitude.
654 This was then used to create maximum and minimum estimates, within which bounds the model’s

655 annual mean rainfall anomaly must lie to suggest enough of an increase to support grassland
656 (Joussaume *et al.* 1999).

657

658 Therefore, an adapted version of Figure 3a in Joussaume *et al.* (1999) is shown in the Supplementary
659 Material (SM7), which shows mean annual rainfall anomalies by latitude (to be consistent with the
660 proxy data-based threshold) from not only the current *midHolocene* simulation, but also all previous
661 MH simulations from CMIP5. Concerning the threshold required to support grassland, it is clear that
662 although the current *midHolocene* simulation is just within the required bounds at lower latitudes (e.g.
663 up to 17°N), north of this the current *midHolocene* simulation is not meeting the required threshold,
664 neither are any of the other CMIP5 models after ~18°N (SM7). It would therefore appear that the
665 ‘Saharan greening’ problem has yet to be resolved, and may well only be reproduced once interactive
666 vegetation, and indeed interactive dust, is included in the simulation; given the current lack of an
667 interactive vegetation/dust model, vegetation-related climate feedbacks (e.g. albedo) on the system are
668 therefore currently missing.

669

670 **4. SUMMARY AND CONCLUSIONS**

671 This study has conducted and assessed the mid-Holocene and Last Interglacial simulations using the
672 latest version of the UK’s physical climate model, HadGEM3-GC3.1, comparing the results firstly
673 with the model’s preindustrial simulation and secondly with previous versions the same model,
674 against available proxy data. Therefore this study is novel, being the first time this version of the UK
675 model has been used to conduct any paleoclimate simulations and therefore being the first time we are
676 in a position to include them as part of the UK’s contribution to CMIP6/PMIP4. Both the
677 *midHolocene* and *lig127k* simulations followed the experimental design defined in Otto-Bliesner *et al.*
678 (2017) and the CMIP6/PMIP4 protocol. Both simulations were run for a 350-400 year spin-up phase,
679 during which atmospheric and oceanic equilibrium were assessed, and once an acceptable level of
680 equilibrium had been reached, the production runs were started.

681

682 Globally, whilst both the recent simulations are mostly capturing the sign and, in some places,
683 magnitude of change relative to the PI, similar to previous model simulations this is geographically
684 and seasonally dependent. It should be noted that the proxy data (against which the simulations are
685 evaluated) also contain a high level of uncertainty in both space and time (in terms of both seasons
686 and geological era), and so it is encouraging that the simulations are generally reproducing the large-
687 scale sign of change, if not at an individual location. Compared to previous versions of the same
688 model, this appears to vary according to metric, proxy reconstruction used for comparison and
689 geographical location. In some instances, such as annual mean rainfall in the MH, there is a clear and
690 linear improvement (relative to proxy data) through the model generations when rainfall is considered
691 globally; likewise there is more accuracy in the two recent versions (again relative to proxy data) than

692 the oldest version when only the West African monsoon region is considered (see Table 4a and the
693 RMSE values discussed in the concluding paragraph of Section 3.1.2).

694

695 Likewise, when zooming into Africa, the behaviour of the West African monsoon in both HadGEM3
696 one climate simulations is consistent with current understanding (e.g. Huang et al. 2001, Singarayer et
697 al. 2017, Wang et al. 2014), which suggests a wetter (and possibly latitudinally wider, and/or
698 northwardly displaced) monsoon during the MH and LIG, relative to the PI. Regarding model
699 development in simulating the West African monsoon, there are differences between model
700 generations; the oldest version of the model, for example, limits the rainfall increases to over sub-
701 Saharan West Africa only, whereas the two most recent versions imply Africa-wide (i.e. across all
702 longitudes) rainfall increases at this same latitude. Lastly, regarding the well-documented ‘Saharan
703 greening’ during the MH, results here suggest that the most recent version of the UK’s physical
704 climate model is consistent with all other previous models to date.

705

706 In conclusion, the results suggest that the most recent version of the UK’s physical climate model is
707 reproducing climate conditions consistent with the known changes to insolation during these two
708 warm periods. Even though the *lig127k* simulation did not contain any influx of Northern
709 Hemisphere meltwater, shown by previous work to be a critical forcing in LIG simulations (causing
710 regions of both warming and cooling, according to location), it is still nevertheless showing increased
711 temperatures in certain regions. Another limitation of using this particular version of the model is
712 that certain processes, such as vegetation and atmospheric chemistry, were prescribed, rather than
713 allowed to be dynamically evolving. Moreover, for practical reasons some of the boundary conditions
714 were left as PI, such as vegetation, anthropogenic deforestation and aerosols; a better simulation
715 might be achieved if these were prescribed for the MH and LIG. Processes and boundary conditions
716 such as these may be of critical importance regarding climate sensitivity during the MH and the LIG,
717 and therefore ongoing work is underway to repeat both of these experiments using the most recent
718 version of the UK’s Earth Systems model, UKESM1. Here, although the atmospheric core is
719 HadGEM3, UKESM1 contains many other earth system components (e.g. dynamic vegetation), and
720 therefore in theory should be able to better reproduce these paleoclimate states.

721

722 **DATA AVAILABILITY**

723 The model simulations will be uploaded in the near future to the Earth System Grid Federation
724 (ESGF) WCRP Coupled Model Intercomparison Project (Phase 6), but are not yet publicly available.
725 The simulations are, however, available by directly contacting the lead author. For the MH
726 reconstructions, the data can be found within the Supplementary Online Material of Bartlein *et al.*
727 (2011), at <https://link.springer.com/article/10.1007/s00382-010-0904-1>. For the LIG temperature
728 reconstructions, the data can be found within the Supplementary Online Material of Capron *et al.*

729 (2017), at <https://www.sciencedirect.com/science/article/pii/S0277379117303487?via%3Dihub>, and
730 the Supplementary Online Material of Hoffman *et al.* (2017), at
731 <https://science.sciencemag.org/content/suppl/2017/01/23/355.6322.276.DC1>. The LIG temperature
732 reconstructions created here, based on the above Hoffman *et al.* (2017) data, are currently available by
733 directly contacting the lead author. For the LIG precipitation reconstructions, the data can be found
734 within the Supplementary Online Material of Scussolini *et al.* (2019), at
735 <https://advances.sciencemag.org/content/suppl/2019/11/18/5.11.eaax7047.DC1>.

736

737 **COMPETING INTERESTS**

738 The authors declare that they have no conflict of interest.

739

740 **AUTHOR CONTRIBUTION**

741 CJRW conducted the *midHolocene* simulation, carried out the analysis, produced the figures, wrote
742 the majority of the manuscript, and led the paper. MVG conducted and provided the *lig127k*
743 simulation, and contributed to some of the analysis and writing. EC provided the proxy data, and
744 contributed to some of the writing. IMV provided the HadCM3 LIG simulation. PJV provided the
745 HadCM3 MH simulation. JS contributed to some of the writing. All authors proofread the
746 manuscript and provided comments.

747

748 **ACKNOWLEDGEMENTS**

749 CJRW acknowledges the financial support of the UK Natural Environment Research Council-funded
750 SWEET project (Super-Warm Early Eocene Temperatures), research grant NE/P01903X/1. CJRW
751 also acknowledges the financial support of the Belmont-funded PACMEDY (PAlaeo-Constraints on
752 Monsoon Evolution and Dynamics) project, as does JS. MVG and LCS acknowledge the financial
753 support of the NERC research grants NE/P013279/1 and NE/P009271/1. EC acknowledges financial
754 support from the ChronoClimate project, funded by the Carlsberg Foundation.

755 **REFERENCES**

- 756 Bartlein, P. J., Harrison, S. P., Brewer, S., et al. (2011). ‘Pollen-based continental climate
757 reconstructions at 6 and 21 ka: a global synthesis’. *Clim. Dyn.* 37: 775–802. DOI:10.1007/s00382-
758 010-0904-1
- 759
- 760 Berger, A. L. (1978). ‘Long-term variations of daily insolation and Quaternary climatic changes’. *J.*
761 *Atmos. Sci.* 35: 2362-2367. [https://doi.org/10.1175/1520-0469\(1978\)035<2362:LTVODI>2.0.CO;2](https://doi.org/10.1175/1520-0469(1978)035<2362:LTVODI>2.0.CO;2)
- 762
- 763 Berger, A. L. & Loutre, M. F. (1991). Insolation values for the climate of the last 10,000,000 years.
764 *Quaternary Sci. Rev.* 10: 297–317. [https://doi.org/10.1016/0277-3791\(91\)90033-Q](https://doi.org/10.1016/0277-3791(91)90033-Q)
- 765
- 766 Braconnot, P., Harrison, S. P., Kageyama, M., et al. (2012). ‘Evaluation of climate models using
767 palaeoclimatic data’. *Nature Climate Change.* 2 (6): 417. DOI: 10.1038/NCLIMATE1456
- 768
- 769 Braconnot, P., Harrison, S. P., Otto-Bliesner, B, et al. (2011). ‘The palaeoclimate modelling
770 intercomparison project contribution to CMIP5’. *CLIVAR Exch. Newsl.* 56: 15–19
- 771
- 772 Braconnot, P., Otto-Bliesner, B., Harrison, S., et al. (2007). ‘Results of PMIP2 coupled simulations
773 of the Mid-Holocene and Last Glacial Maximum – Part 1: experiments and large-scale features’.
774 *Clim. Past.* 3: 261-277. <https://doi.org/10.5194/cp-3-261-2007>
- 775
- 776 Brierley, C. M., Zhao, A., Harrison, S., et al. (2020). ‘Large-scale features and evaluation of the
777 PMIP4-CMIP6 midHolocene simulations’. *Clim. Past.* Under review
- 778
- 779 Capron, E., Govin, A., Stone, E. J., et al. (2014). ‘Temporal and spatial structure of multi-millennial
780 temperature changes at high latitudes during the Last Interglacial’. *Quat. Sci. Rev.* 103: 116-133.
781 <https://doi.org/10.1016/j.quascirev.2014.08.018>
- 782
- 783 Capron, E., Govin, A., Feng R. et al. (2017). ‘Critical evaluation of climate syntheses to benchmark
784 CMIP6/PMIP4 127 ka Last Interglacial simulations in the high-latitude regions’. *Quat. Sci. Rev.*
785 168: 137-150. DOI: 10.1016/j.quascirev.2017.04.019
- 786
- 787 Carlson, A. E. (2008). ‘Why there was not a Younger Dryas-like event during the Penultimate
788 Deglaciation’. *Quaternary Sci. Rev.* 27: 882-887. DOI: 10.1016/j.quascirev.2008.02.004
- 789

790 Drake, N. A., Blench, R. M., Armitage, S. J., et al. (2011). ‘Ancient watercourses and biogeography
791 of the Sahara explain the peopling of the desert’. *Proceedings of the National Academy of Sciences*.
792 108 (2): 458-462. DOI: 10.1073/pnas.1012231108
793

794 Fischer, H., Meissner, K. J., Mix, A. C. et al. (2018). ‘Palaeoclimate constraints on the impact of 2°C
795 anthropogenic warming and beyond’. *Nature Geoscience*. 11: 474-485.
796 <https://doi.org/10.1038/s41561-018-0146-0>
797

798 Gates, W. L. (1976). ‘The numerical simulation of ice-age climate with a global general circulation
799 model’. *J. Atmos. Sci.* 33: 1844–1873. DOI: 10.1175/1520-
800 0469(1976)033<1844:TNSOIA>2.0.CO;2
801

802 Gregoire, L. J., Valdes, P. J., Payne, A. J. & Kahana, R. (2011). ‘Optimal tuning of a GCM using
803 modern and glacial constraints’. *Clim Dyn.* 37: 705-719. DOI:10.1007/s00382-010-0934-8
804

805 Guarino, M. V., Sime, L., Schroeder, D., et al. (2020a). ‘Machine dependence and reproducibility for
806 coupled climate simulations: The HadGEM3-GC3.1 CMIP Preindustrial simulation’. *GMD*. 13 (1):
807 139-154. <https://doi.org/10.5194/gmd-2019-83>
808

809 Guarino, M. V. et al. (2020b). ‘A sea ice-free Arctic during the Last Interglacial supports fast future
810 loss’. *Nature Climate Change*. Under review
811

812 Gunnar, M., Highwood, E. J., Shin, K. P. & Stordal, F. (1998) "New estimates of radiative forcing
813 due to well mixed greenhouse gases.". *Geophys. Res. Lett.* 25 (14): 2715-2718.
814 <https://doi.org/10.1029/98GL01908>
815

816 Harrison, S. P., Bartlein, P. J., Brewer, S., et al. (2014). ‘Climate model benchmarking with glacial
817 and mid-Holocene climates’. *Clim. Dyn.* 43: 671–688. <https://doi.org/10.1007/s00382-013-1922-6>
818

819 Harrison, S. P., Bartlein, P. J., Izumi, K., et al. (2015). ‘Evaluation of CMIP5 palaeo-simulations to
820 improve climate projections’. *Nature Climate Change*. 5: 735. DOI: 10.1038/nclimate2649
821

822 Haxeltine, A. & Prentice, I. C. (1996). ‘BIOME3: an equilibrium terrestrial biosphere model based on
823 ecophysiological constraints, resource availability, and competition among plant functional types’.
824 *Global Biogeochemical Cycles*. 10 (4): 693-709. DOI: 10.1029/96GB02344
825

826 Haywood, A. M., Dowsett, H. J., Dolan, A. M. et al. (2016). ‘The Pliocene Model Intercomparison
827 Project (PlioMIP) Phase 2: scientific objectives and experimental design’. *Clim. Past.* 12: 663-675.
828 <https://doi.org/10.5194/cp-12-663-2016>
829

830 Haug, G., Hughen, K. A., Sigman, D. M., et al. (2001). ‘Southward migration of the intertropical
831 convergence zone through the Holocene’. *Science.* 293: 1304-1308. DOI: 10.1126/science.1059725
832

833 Hoelzmann, P., Jolly, D., Harrison, S. P., et al. (1998). ‘Mid-Holocene land-surface conditions in
834 northern Africa and the Arabian Peninsula: A data set for the analysis of biogeophysical feedbacks in
835 the climate system’. *Global Biogeochemical Cycles.* 12 (1): 35-51.
836 <https://doi.org/10.1029/97GB02733>
837

838 Hoffman, J. S., Clark, P. U., Parnell, A. C., et al. (2017). ‘Regional and global sea-surface
839 temperatures during the last interglaciation’. *Science.* 355: 276-279. DOI: 10.1126/science.aai8464
840

841 Hollingsworth, A., Kållberg, P., Renner, V. & Burridge, D. M. (1983). ‘An internal symmetric
842 computational instability’. *QJRMS.* 109: 417–428. <https://doi.org/10.1002/qj.49710946012>
843

844 Holloway, M. D., Sime, L. C., Singarayer, J. S., et al. (2016). ‘Antarctic last interglacial isotope peak
845 in response to sea ice retreat not ice-sheet collapse’. *Nature Comms.* 7: 12293.
846 <https://doi.org/10.1038/ncomms12293>
847

848 Jungclaus, J. H., Bard, E., Baroni, M. et al. (2017). ‘The PMIP4 contribution to CMIP6 – Part 3: The
849 last millennium, scientific objective, and experimental design for the PMIP4 past1000 simulations’.
850 *GMD.* 10: 4005-4033. <https://doi.org/10.5194/gmd-10-4005-2017>
851

852 Jolly, D., Harrison, S. P., Damnati, B. & Bonnefille, R. (1998a). ‘Simulated climate and biomes of
853 Africa during the Late Quaternary: Comparison with pollen and lake status data’. *Quat. Sci. Rev.* 17
854 (6-7): 629-657. [https://doi.org/10.1016/S0277-3791\(98\)00015-8](https://doi.org/10.1016/S0277-3791(98)00015-8)
855

856 Jolly, D., Prentice, I. C., Bonnefille, R. et al. (1998b). ‘Biome reconstruction from pollen and plant
857 macrofossil data for Africa and the Arabian peninsula at 0 and 6000 years’. *J. Biogeography.* 25 (6):
858 1007-1027
859

860 Joussaume, S. & Braconnot, P. (1997). ‘Sensitivity of paleoclimate simulation results to season
861 definitions’. *J. Geophys. Res.-Atmos.* 102: 1943-1956
862

863 Joussaume, S. & Taylor K. E. (1995). 'Status of the Paleoclimate Modeling Intercomparison Project'.
864 In: Proceedings of the First International AMIP Scientific Conference, WCRP-92 425. 430 Monterey,
865 USA
866

867 Joussaume, S., Taylor, K. E., Braconnot, P. et al. (1999). 'Monsoon changes for 6000 years ago:
868 Results of 18 simulations from the Paleoclimate Modeling Intercomparison Project (PMIP)'. *GRL*.
869 26 (7): 859-862. <https://doi.org/10.1029/1999GL900126>
870

871 Kageyama, M., Albani, S., Braconnot, P. et al. (2017). 'The PMIP4 contribution to CMIP6 – Part 4:
872 Scientific objectives and experimental design of the PMIP4-CMIP6 Last Glacial Maximum
873 experiments and PMIP4 sensitivity experiments'. *GMD*. 10: 4035-4055.
874 <https://doi.org/10.5194/gmd-10-4035-2017>
875

876 Kageyama, M., Braconnot, P., Harrison, S. P. et al. (2018). 'The PMIP4 contribution to CMIP6 –
877 Part 1: Overview and over-arching analysis plan'. *GMD*. 11: 1033-1057.
878 <https://doi.org/10.5194/gmd-11-1033-2018>
879 Kuhlbrodt, T., Jones, C. G., Sellar, A. et al. (2018). 'The
880 low resolution version of HadGEM3 GC3.1: Development and evaluation for global climate'. *J. Adv.
881 Model. Earth Sy.* 10: 2865-2888. <https://doi.org/10.1029/2018MS001370>
882

882 Kutzbach, J. E., Liu, X., Liu, Z. & Chen, G. (2008). 'Simulation of the evolutionary response of
883 global summer monsoons to orbital forcing over the past 280,000 years'. *Clim. Dyn.* 30: 567-579.
884 DOI: 10.1007/s00382-007-0308-z
885

886 Kohfeld, K. E., Graham, R. M., de Boer, A. M. et al. (2013). 'Southern Hemisphere westerly wind
887 changes during the Last Glacial Maximum: paleo-data synthesis'. *Quat. Sci. Rev.* 68: 76-95.
888 <https://doi.org/10.1016/j.quascirev.2013.01.017>
889

890 Lézine, A. M., Hély, C., Grenier, C. et al. (2011). 'Sahara and Sahel vulnerability to climate changes,
891 lessons from Holocene hydrological data'. *Quat. Sci. Rev.* 30 (21-22): 3001-3012.
892 DOI:10.1016/j.quascirev.2011.07.006
893

894 Liu, Z., Zhu, J., Rosenthal, Y. et al. (2014). 'The Holocene temperature conundrum'. *PNAS*. 111
895 (34): 3501-3505. DOI: 10.1073/pnas.1407229111
896

897 Lunt, D. J., Abe-Ouchi, A., Bakker, P. et al. (2013). 'A multi-model assessment of last interglacial
898 temperatures'. *Clim. Past*. 9: 699–717. <https://doi.org/10.5194/cp-9-699-2013>
899

900 Lunt, D. J., Foster, G. L., Haywood, A. M. & Stone, E. J. (2008). ‘Late Pliocene Greenland
901 glaciation controlled by a decline in atmospheric CO₂ levels’. *Nature*. 454 (7208): 1102. DOI:
902 10.1038/nature07223.
903

904 Marcott, S. A., Shakun, J. D., Clark, P. U. & Mix, A. C. (2013). ‘A reconstruction of regional and
905 global temperature for the past 11,300 years’. *Science*. 399 (6124): 1198-1201. DOI:
906 10.1126/science.1228026.
907

908 Marzocchi, A., Lunt, D. J., Flecker, R. et al. (2015). ‘Orbital control on late Miocene climate and the
909 North African monsoon: insight from an ensemble of sub-precessional simulations’. *Clim. Past*. 11
910 (10): 1271-1295. <https://doi.org/10.5194/cp-11-1271-2015>
911

912 McGee, D., Donohoe, A., Marshall, J. & Ferreira, D. (2014). ‘Changes in ITCZ location and cross-
913 equatorial heat transport at the Last Glacial Maximum, Heinrich Stadial 1, and the Mid-Holocene’.
914 *Earth and Planetary Science Letters*. 390: 69-79. <https://doi.org/10.1016/j.epsl.2013.12.043>
915

916 Menary, M. B., Kuhlbrodt, T., Ridley, J. et al. (2018). ‘Pre-industrial control simulations with
917 HadGEM3-GC3.1 for CMIP6’. *JAMES*. 10: 3049–3075. <https://doi.org/10.1029/2018MS001495>
918

919 New, M., Lister, D., Hulme, M. & Makin, I. (2002). ‘A high-resolution data set of surface climate
920 over global land areas’. *Clim Res*. 21: 2217–2238. DOI:10.3354/cr021001
921

922 Otto-Bliesner, B. L., Braconnot, P., Harrison, S. P. et al. (2017). ‘The PMIP4 contribution to CMIP6
923 – Part 2: Two interglacials, scientific objective and experimental design for Holocene and Last
924 Interglacial simulations’. *GMD*. 10: 3979-4003. <https://doi.org/10.5194/gmd-10-3979-2017>
925

926 Pollard, D. & Reusch, D. B. (2002). ‘A calendar conversion method for monthly mean paleoclimate
927 model output with orbital forcing’. *J. Geophys. Res.* 107 (D22). DOI:10.1029/2002JD002126
928

929 Rachmayani, R., Prange, M., Lunt, D. J., et al. (2017). ‘Sensitivity of the Greenland Ice Sheet to
930 interglacial climate forcing: MIS 5e versus MIS11’. *Paleoceanography*. 32 (11): 1089-1101.
931 <https://doi.org/10.1002/2017PA003149>
932

933 Ramstein, G., Fluteau, F., Besse, J. & Joussaume, S. (1997). ‘Effect of orogeny, plate motion and
934 land–sea distribution on Eurasian climate change over the past 30 million years’. *Nature*. 386 (6627):
935 788. <https://doi.org/10.1038/386788a0>
936

937 Ridley, J., Blockley, E., Keen, A. B. et al. (2017). ‘The sea ice model component of HadGEM3-
938 GC3.1’. *GMD*. 11: 713-723. <https://doi.org/10.5194/gmd-11-713-2018>
939

940 Rind, D. & Peteet, D. (1985). ‘Terrestrial conditions at the last glacial maximum and CLIMAP sea-
941 surface temperature estimates: Are they consistent?’ *Quat. Res.* 2: 1-22. DOI:10.1016/0033-
942 5894(85)90080-8
943

944 Schmidt, G. A., Annan, J. D., Bartlein, P. J. et al. (2014). ‘Using paleo-climate comparisons to
945 constrain future projections in CMIP5’. *Clim. Past.* 10: 221-250. [https://doi.org/10.5194/cp-10-221-](https://doi.org/10.5194/cp-10-221-2014)
946 2014

947 Scussolini, P., Bakker, P., Guo, C. et al. (2019). ‘Agreement between reconstructed and modeled
948 boreal precipitation of the Last Interglacial’. *Sci. Adv.* 5 (11): 1-11.
949 DOI: 10.1126/sciadv.aax7047
950

951 Singarayer, J. S. & Burrough, S. L. (2015). ‘Interhemispheric dynamics of the African rainbelt during
952 the late Quaternary’. *Quaternary Science Reviews.* 124: 48-67.
953 DOI: 10.1016/j.quascirev.2015.06.021
954

955 Singarayer, J. S., Valdes, P. J. & Roberts, W. H. G. (2017). ‘Ocean dominated expansion and
956 contraction of the late Quaternary tropical rainbelt’. *Nature Scientific Reports.* 7: 9382.
957 DOI:10.1038/s41598-017-09816-8
958

959 Smith, R. S. & Gregory, J. M. (2009). ‘A study of the sensitivity of ocean overturning circulation and
960 climate to freshwater input in different regions of the North Atlantic’. *Geophys. Res. Lett.* 36.
961 DOI:10.1029/2009GL038607
962

963 Stone, E. J., Capron, E., Lunt, D. J., et al. (2016). ‘Impact of meltwater on high-latitude early Last
964 Interglacial climate’. *Clim. Past.* 12: 1919–1932. <https://doi.org/10.5194/cp-12-1919-2016>
965

966 Storkey, D., Megann, A., Mathiot, P. et al. (2017). ‘UK Global Ocean GO6 and GO7: A traceable
967 hierarchy of model resolutions’. *GMD*. 11: 3187-3213. <https://doi.org/10.5194/gmd-11-3187-2018>
968

969 Taylor, K. E., Stouffer, R. J. & Meehl, G. A. (2011). ‘An overview of CMIP5 and the experiment
970 design’. *Bull. Am. Meteorol. Soc.* 93: 485-498. <https://doi.org/10.1175/BAMS-D-11-00094.1>
971

972 Turney, C. S. M. & Jones, R. T. (2010). ‘Does the Agulhas Current amplify global temperatures
973 during super-interglacials?’ *J. Quat. Sci.* 25 (6): 839-843. <https://doi.org/10.1002/jqs.1423>
974

975 Walters, D. N., A., Baran, I., Boutle, M. E. et al. (2017). ‘The Met Office Unified Model Global
976 Atmosphere 7.0/7.1 and JULES Global Land 7.0 configurations’. *GMD.* 12: 1909-1923.
977 <https://doi.org/10.5194/gmd-12-1909-2019>
978

979 Wang, X., et al. (2006). ‘Interhemispheric anti-phasing of rainfall during the last glacial period’.
980 *Quat. Sci. Rev.* 25: 3391-3403. DOI: 10.1016/j.quascirev.2006.02.009
981

982 Wang, Y., Cheng, H., Edwards, R.L., et al. (2008). ‘Millennial-and orbital-scale changes in the East
983 Asian monsoon over the past 224,000 years’. *Nature.* 451 (7182): 1090. DOI: 10.1038/nature06692
984

985 Wang, P. X., et al. (2014). ‘The global monsoon across timescales: coherent variability of regional
986 monsoons’. *Clim. Past.* 10: 2007-2052. <https://doi.org/10.5194/cp-10-2007-2014>
987

988 Williams, K. D., Copsey, D., Blockley E. W., et al. (2017). ‘The Met Office Global Coupled Model
989 3.0 and 3.1 (GC3.0 and GC3.1) Configurations’. *JAMES.* 10 (2): 357-380.
990 <https://doi.org/10.1002/2017MS001115>
991

992 **LIST OF TABLES**

993 Table 1 - Astronomical parameters and atmospheric trace gas concentrations used in HadGEM3
994 *midHolocene* and *lig127k* simulations

995

996 Table 2 - Trends (per century) in global mean measures of climate equilibrium for the last hundred
997 years of the simulations, adapted from and including *piControl* results from Menary *et al.* (2018)

998

999 Table 3 - Global 1.5 m air temperature means and anomalies from HadGEM3 *piControl*,
1000 *midHolocene* and *lig127k* production runs

1001

1002 Table 4 - RMSE values (for various metrics) between simulations from different generations of the
1003 same model versus proxy data, and versus each other: a) MAT and MAP from the MH simulations
1004 versus proxy data from Bartlein *et al.* (2011); b) SST from the LIG simulations versus proxy data
1005 from Capron *et al.* (2017) and Hoffman *et al.* (2017). Regarding the proxy data comparisons in b), for
1006 JAS the simulated SST anomalies are compared to Northern Hemisphere summer reconstructions and
1007 for JFM the simulated SST anomalies are compared to Southern Hemisphere summer reconstructions

1008

1009 **LIST OF FIGURES**

1010 Figure 1 - Calendar adjusted latitude-month insolation (incoming SW radiative flux) anomalies: a)
1011 *midHolocene - piControl*; b) *lig127k - piControl*

1012

1013 Figure 2 - Calendar adjusted 1.5 m air temperature climatology differences, HadGEM3 *midHolocene*
1014 and *lig127k* production runs versus HadGEM3 *piControl* production run: a-c) *midHolocene -*
1015 *piControl*; d-f) *lig127k - piControl*. Top row: Annual; Middle row: Northern Hemisphere summer
1016 (JJA); Bottom row: Northern Hemisphere winter (DJF). Stippling shows statistical significance (as
1017 calculated by a Student's T-test) at the 99% level

1018

1019 Figure 3 - Same as Figure 2, but for daily surface rainfall differences

1020

1021 Figure 4 - Annual mean meridional overturning streamfunction climatologies from HadGEM3: a-c)
1022 Atlantic basin; d-f) Global. Top row: *piControl* simulation; Middle row: *midHolocene* simulation;
1023 Bottom row: *lig127k* simulation

1024

1025 Figure 5 - Calendar adjusted JJA daily surface rainfall & 850mb wind climatology differences,
1026 HadGEM3 *midHolocene* and *lig127k* production runs versus HadGEM3 *piControl* production run: a)
1027 *midHolocene - piControl*; b) *lig127k - piControl*; c) *lig127k - midHolocene*

1028

1029 Figure 6 - Calendar adjusted JJA daily rainfall climatology by latitude, averaged over West Africa
1030 (20°W-15°E, land points only), for the various generations of the UK's physical climate model: a)
1031 Absolute values; b) Anomalies (MH or LIG – PI). Solid lines show PI simulations, dashed lines show
1032 MH simulations and dotted lines show LIG simulations
1033

1034 Figure 7 - Calendar adjusted mean annual surface air temperature anomalies from simulated model
1035 data versus proxy data. Background data show simulated anomalies (MH – PI) from different
1036 generations of the same model: a) Proxy data anomalies (MH – PI) from Bartlein et al. (2011), with
1037 locations projected onto model grid; b) HadGEM3; c) HadGEM2-ES; d) HadCM3
1038

1039 Figure 8 - Same as Figure 7, but for rainfall anomalies
1040

1041 Figure 9 - Calendar adjusted SST anomalies from model simulated data versus proxy data.
1042 Background data show simulated anomalies (LIG - PI climatology) from different generations of the
1043 same model, circles show proxy data anomalies (LIG – preindustrial) from Capron et al. (2017) and
1044 triangles show anomalies from Hoffman et al. (2017). Proxy data locations are projected onto model
1045 grid: a-c) HadGEM3; d-f) HadCM3. Top row: Annual; Middle row: Northern Hemisphere summer
1046 (JAS); Bottom row: Southern Hemisphere summer (JFM)
1047

1048 Figure 10 - Calendar adjusted annual surface rainfall anomalies from model simulated data versus
1049 proxy data. Background data show simulated anomalies (LIG - PI climatology) from different
1050 generations of the same model, circles show proxy data anomalies (LIG – preindustrial) from
1051 Scussolini et al. (2019). Proxy data locations are projected onto model grid: a) HadGEM3; b)
1052 HadCM3. Inset shows semi-quantitative scale of proxy data, adapted from Scussolini et al. (2019)
1053
1054
1055

1056 **LIST OF SUPPLEMENTARY MATERIAL FIGURES**

1057 SM1 - Latitude-month insolation (incoming SW radiative flux) anomalies, using modern
1058 calendar: a) *midHolocene - piControl*; b) *lig127k - piControl*

1059

1060 SM2 - Annual global mean atmospheric fields from HadGEM3 *piControl*, *midHolocene* and *lig127k*
1061 spin-up phases: a) 1.5 m air temperature; b) TOA radiation balance. Thin lines in b) show annual
1062 TOA radiation balance, thick lines show 11-year running mean. Note that the *piControl* spin-up
1063 phase was run in three separate parts, to accommodate for minor changes/updates in the model as the
1064 simulation progressed. Note also that the first ~50 years of the *lig127k* simulation have been
1065 deliberately removed from this figure, because a number of model crashes caused the model to be
1066 initially unstable and give highly varied global mean temperatures.

1067

1068 SM3 - Centennial trends in 1.5m temperature for HadGEM3 warm climate simulations' spin-up
1069 phases, last 100 years only: a) *midHolocene* ; b) *lig127k*. Stippling shows statistical significance (as
1070 calculated by a Mann-Kendall test) at the 99% level

1071

1072 SM4 - Annual global mean (full depth) oceanic fields from HadGEM3 *piControl*, *midHolocene* and
1073 *lig127k* spin-up phases: a) OceTemp; b) OceSal

1074

1075 SM5 - Modern calendar 1.5 m air temperature climatology differences, HadGEM3 *midHolocene* and
1076 *lig127k* production runs versus HadGEM3 *piControl* production run: a) *midHolocene - piControl*,
1077 JJA; b) *midHolocene - piControl*, DJF; c) *lig127k - piControl*, JJA; d) *lig127k - piControl*, DJF.
1078 Stippling shows statistical significance (as calculated by a Student's T-test) at the 99% level

1079

1080 SM6 - Annual mean sea-ice climatology differences, HadGEM3 *midHolocene* production run versus
1081 HadGEM3 *piControl* production run. Stippling shows statistical significance (as calculated by a
1082 Student's T-test) at the 99% level

1083

1084 SM7 - Annual mean rainfall over West Africa (averaged over 20°W-30°E, consistent with Joussaume
1085 *et al.* [1999]), HadGEM3 *midHolocene* simulation minus corresponding *piControl*, and likewise for
1086 previous models from CMIP5. Solid line shows HadGEM3, dotted lines show CMIP5 simulations.
1087 Grey dashes show maximum and minimum bounds of the increase in rainfall required to support
1088 grassland at each latitude, within which simulations must lie if producing enough rainfall to support
1089 grassland (adapted from Figure 3a in Joussaume *et al.* [1999])

1090

1091

1092 TABLES

	<i>piControl</i>	<i>midHolocene</i>	<i>lig127k</i>
Astronomical parameters			
Eccentricity	0.016764	0.018682	0.039378
Obliquity	23.459	24.105°	24.04°
Perihelion-180°	100.33	0.87°	275.41°
Date of vernal equinox	March 21 at noon	March 21 at noon	March 21 at noon
Trace gases			
CO₂	284.3 ppm	264.4 ppm	275 ppm
CH₄	808.2 ppb	597 ppb	685 ppb
N₂O	273 ppb	262 ppb	255 ppb
Other GHG gases	CMIP DECK <i>piControl</i>	CMIP DECK <i>piControl</i>	CMIP DECK <i>piControl</i>

1093

1094 Table 1 - Astronomical parameters and atmospheric trace gas concentrations used in HadGEM3
1095 simulations

1096

1097

1098

Variable	<i>piControl</i>	<i>midHolocene</i>	<i>lig127k</i>
TOA (W m²)	-0.002	-0.05	-0.06
1.5 m air temp (°C)	0.03	-0.06	-0.16
OceTemp (°C)	0.035	0.03	0.03
OceSal (psu)	0.0001	-0.0004	0.00007

1099

1100 Table 2 - Trends (per century) in global mean measures of climate equilibrium for the last hundred
1101 years of the simulations, adapted from and including *piControl* results from Menary *et al.* (2018)

1102

1103

Time period	Means (°C)			Anomalies (°C)	
	<i>piControl</i>	<i>midHolocene</i>	<i>lig127k</i>	<i>midHolocene – piControl</i>	<i>lig127k – piControl</i>
Annual	13.8	13.67	14.29	-0.12	0.49
JJA	15.68	15.75	17.37	0.07	1.69
DJF	11.86	11.55	11.39	-0.31	-0.47

1104

1105 Table 3 - Global 1.5 m air temperature means and anomalies from HadGEM3 *piControl*,
1106 *midHolocene* and *lig127k* production runs

1107

1108

1109

1110

1111

1112

1113

1114

1115

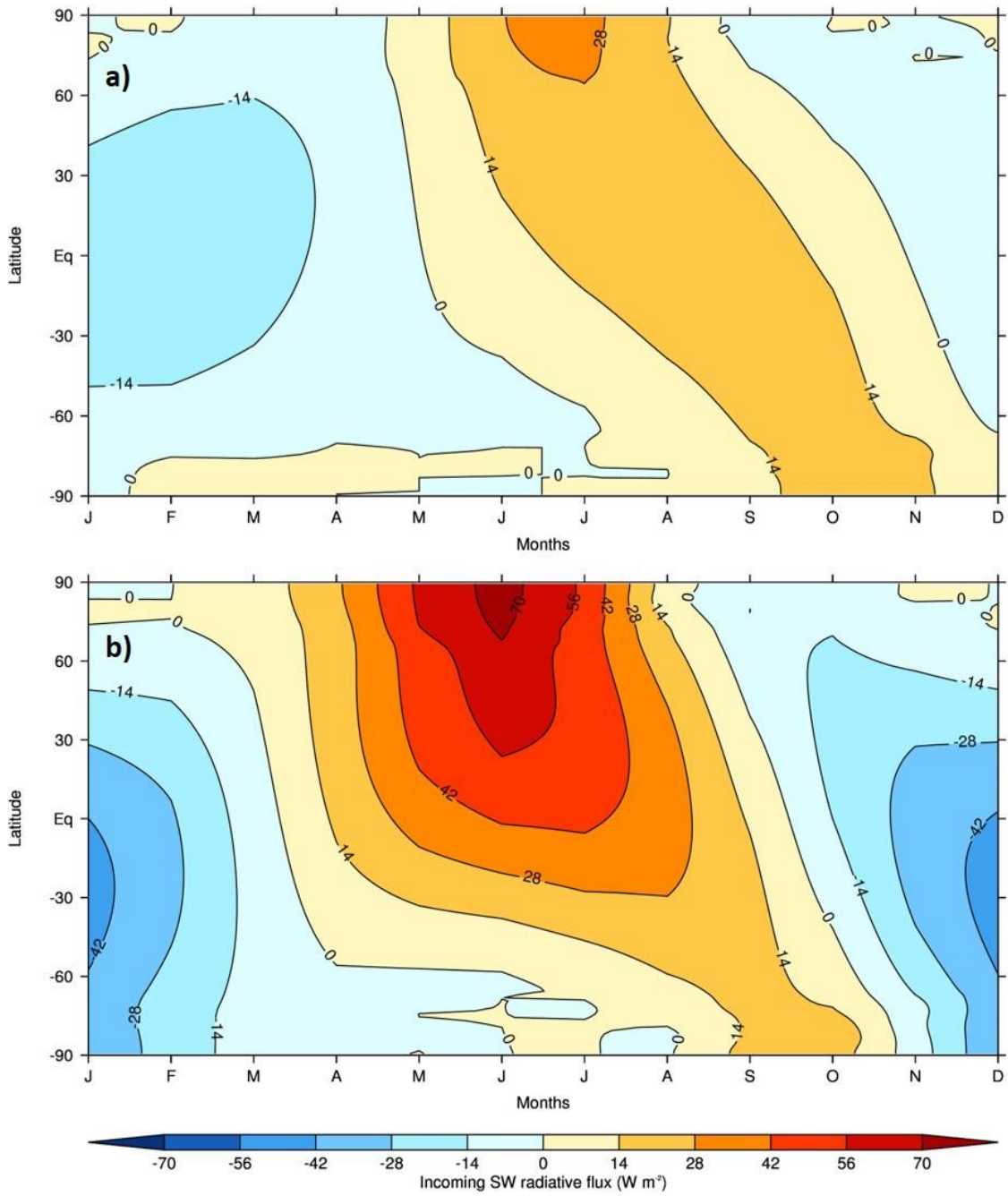
1116 a)
1117

Metric	Simulations vs proxy data			Simulations vs simulations	
	HadGEM3	HadGEM2-ES	HadCM3	HadGEM2-ES v HadGEM3	HadCM3 v HadGEM3
MAT (°C)	2.45	2.42	2.37	0.65	0.57
<i>No. of locations</i>	638			<i>Global coverage</i>	
MAP (mm year⁻¹)	285.9	293.5	304.7	90.8	121.8
<i>No. of locations</i>	651			<i>Global coverage</i>	

1118
1119 b)
1120

Metric	Simulations vs proxy data					
	Yearly		JAS		JFM	
	HadGEM3	HadCM3	HadGEM3	HadCM3	HadGEM3	HadCM3
SST from Capron <i>et al.</i> (2017)	3.03	3.04	3.03	2.98	2.81	2.62
<i>No. of locations</i>	3		24		15	
SST from Hoffman <i>et al.</i> (2017)	2.42	3.02	1.99	2.78	4.28	3.97
<i>No. of locations</i>	86		12		6	

1121
1122 Table 4 - RMSE values (for various metrics) between simulations from different generations of the
1123 same model versus proxy data, and versus each other: a) MAT and MAP from the MH simulations
1124 versus proxy data from Bartlein *et al.* (2011); b) SST from the LIG simulations versus proxy data
1125 from Capron *et al.* (2017) and Hoffman *et al.* (2017). Regarding the proxy data comparisons in b), for
1126 JAS the simulated SST anomalies are compared to Northern Hemisphere summer reconstructions and
1127 for JFM the simulated SST anomalies are compared to Southern Hemisphere summer reconstructions
1128
1129
1130

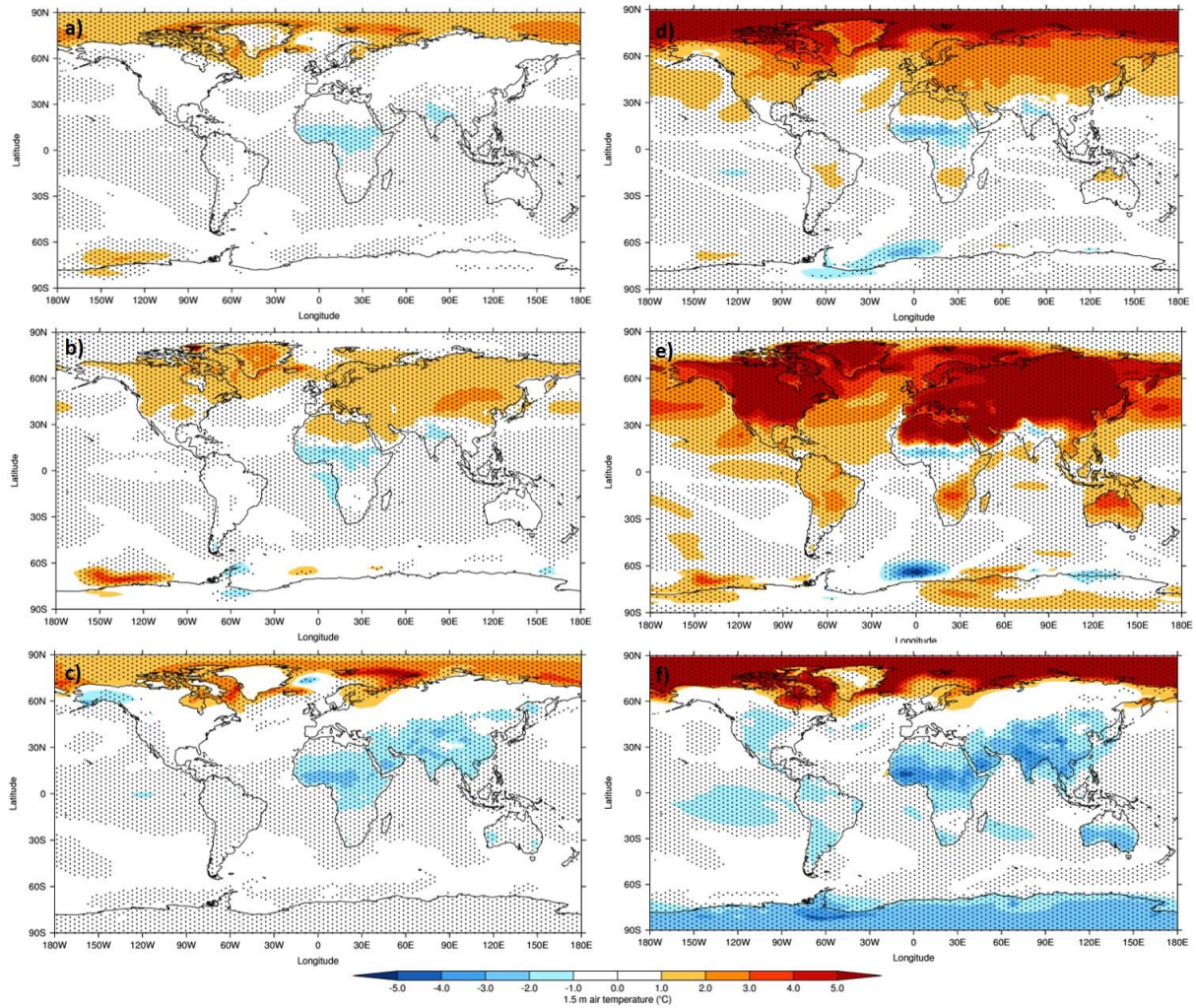


1132

1133 Figure 1 - Calendar adjusted latitude-month insolation (incoming SW radiative flux) anomalies: a)

1134 *midHolocene - piControl*; b) *lig127k - piControl*

1135



1136

1137 Figure 2 - Calendar adjusted 1.5 m air temperature climatology differences, HadGEM3 *midHolocene*

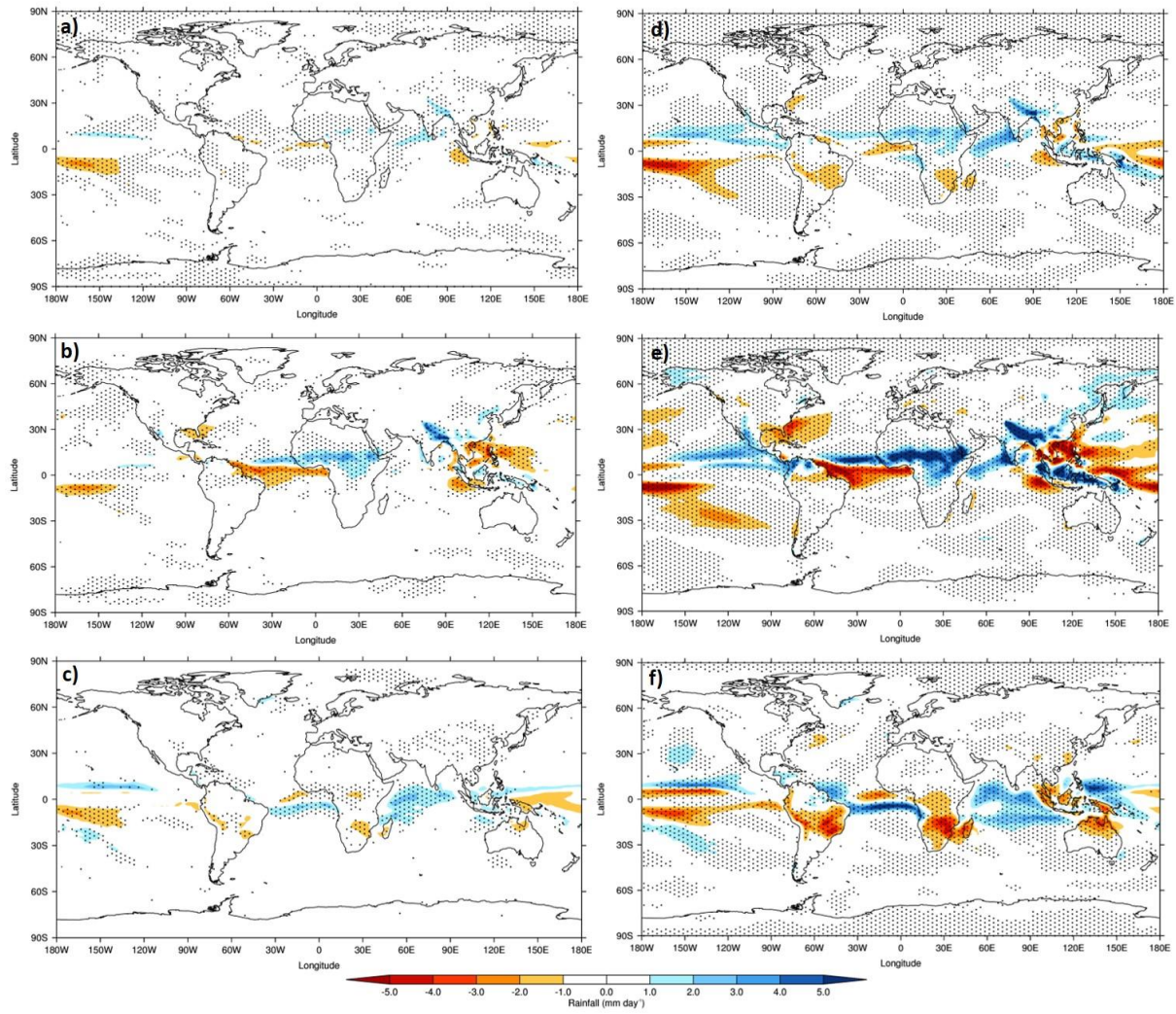
1138 and *lig127k* production runs versus HadGEM3 *piControl* production run: a-c) *midHolocene* –

1139 *piControl*; d-f) *lig127k* – *piControl*. Top row: Annual; Middle row: Northern Hemisphere summer

1140 (JJA); Bottom row: Northern Hemisphere winter (DJF). Stippling shows statistical significance (as

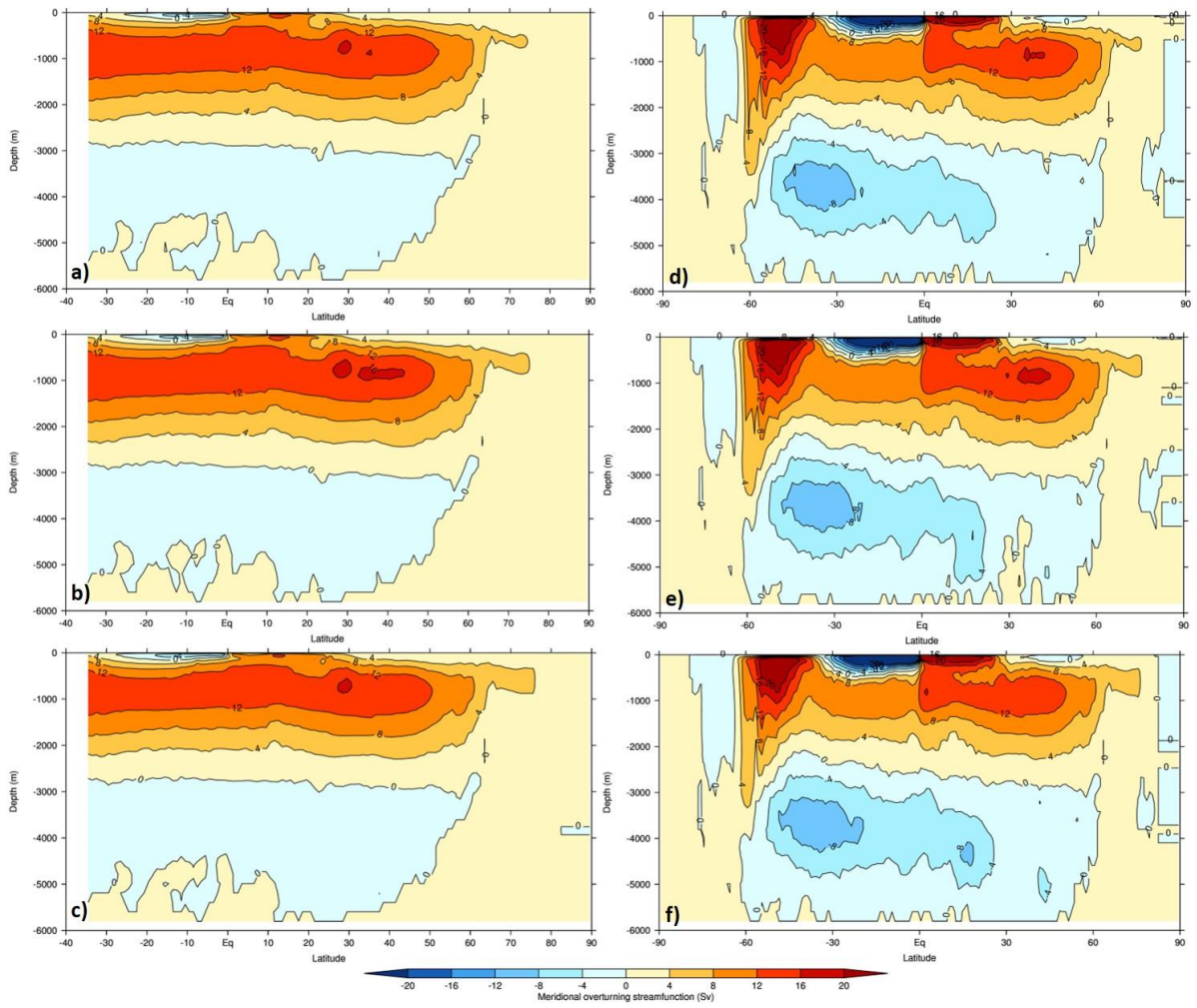
1141 calculated by a Student's T-test) at the 99% level

1142



1143

1144 Figure 3 - Same as Figure 2, but for daily surface rainfall differences



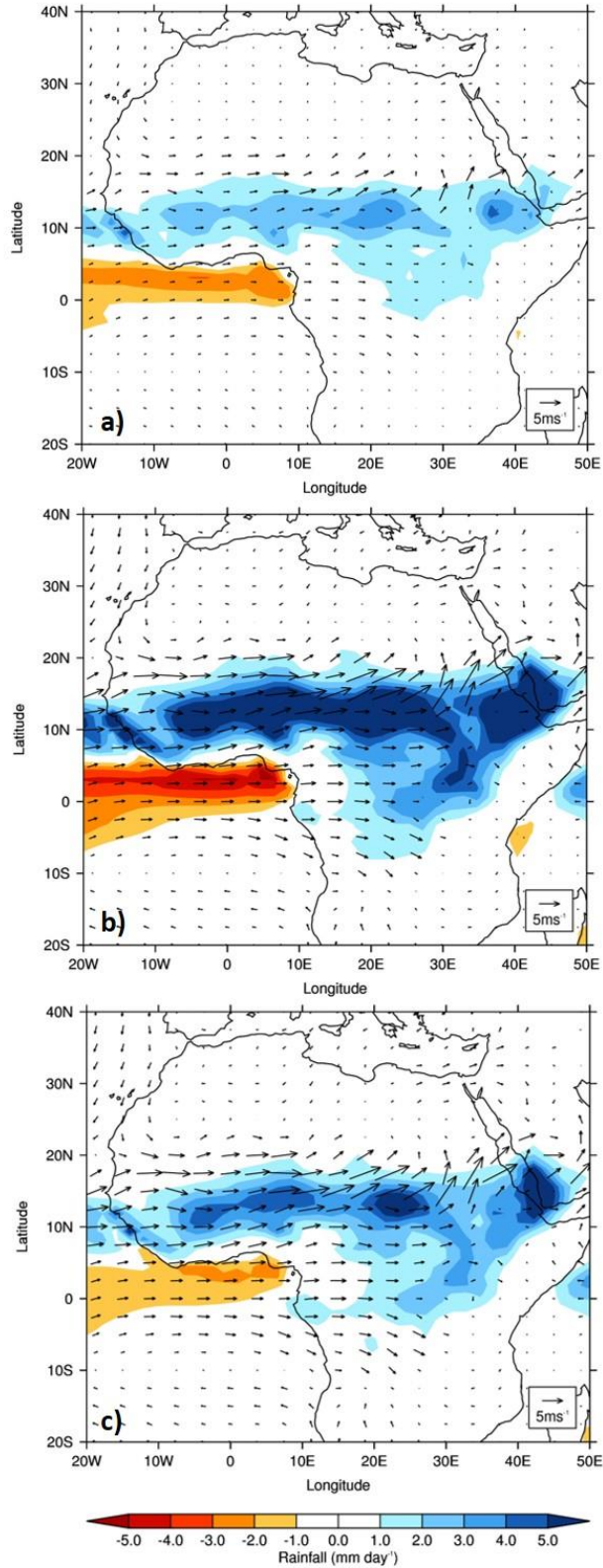
1145

1146 Figure 4 - Annual mean meridional overturning streamfunction climatologies from HadGEM3: a-c)

1147 Atlantic basin; d-f) Global. Top row: *piControl* simulation; Middle row: *midHolocene* simulation;

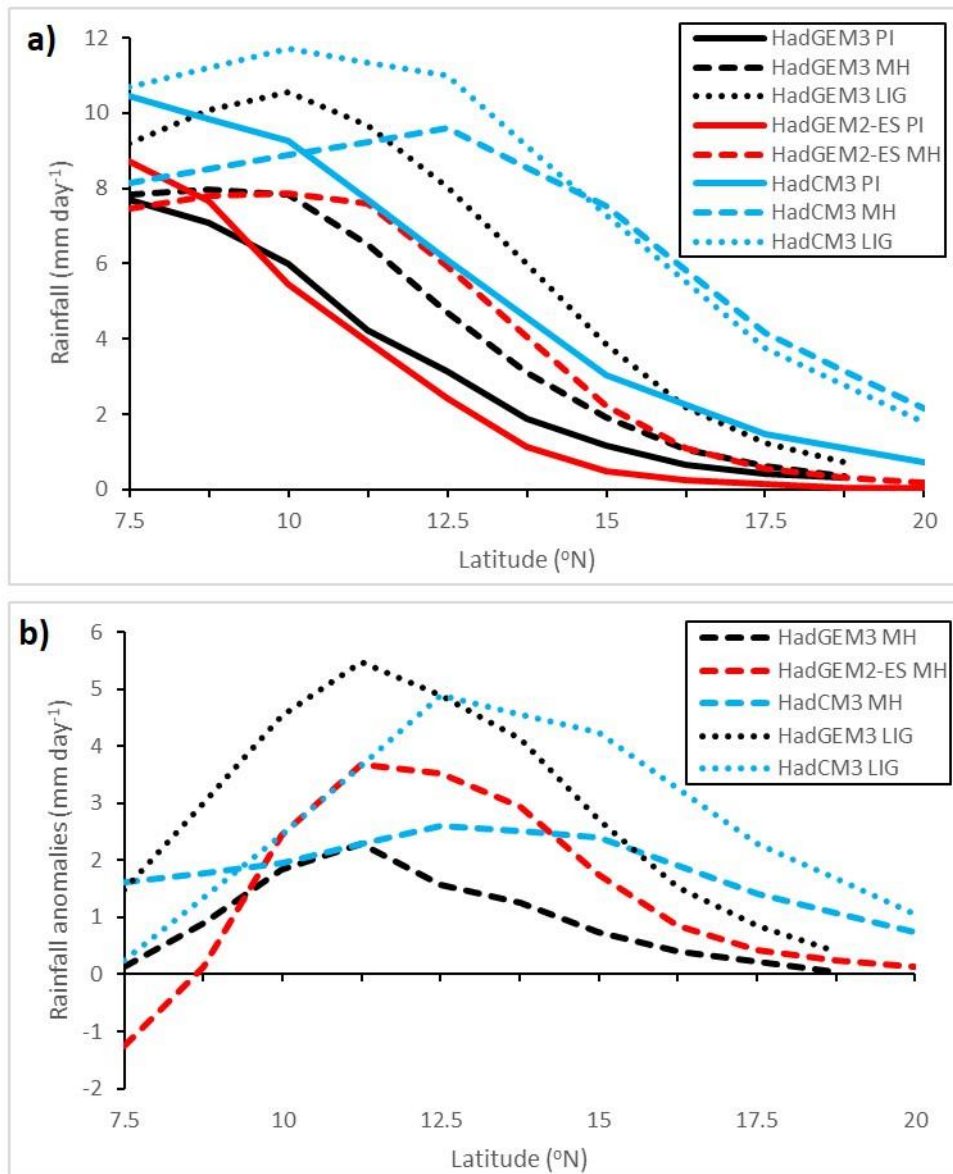
1148 Bottom row: *lig127k* simulation

1149



1150

1151 Figure 5 - Calendar adjusted JJA daily surface rainfall and 850mb wind climatology differences,
 1152 HadGEM3 *midHolocene* and *lig127k* production runs versus HadGEM3 *piControl* production run: a)
 1153 *midHolocene* – *piControl*; b) *lig127k* – *piControl*; c) *lig127k* – *midHolocene*



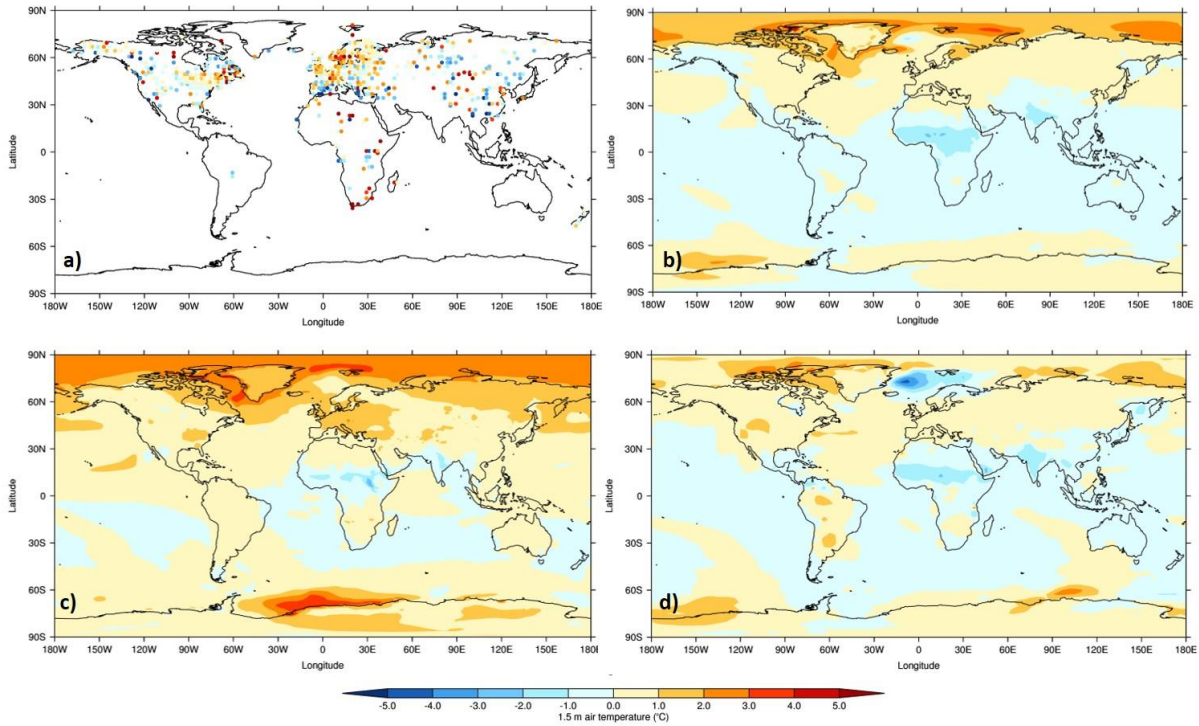
1154

1155 Figure 6 - Calendar adjusted JJA daily rainfall climatology by latitude, averaged over West Africa

1156 (20°W-15°E, land points only), for the various generations of the UK's physical climate model: a)

1157 Absolute values; b) Anomalies (MH or LIG – PI). Solid lines show PI simulations, dashed lines show

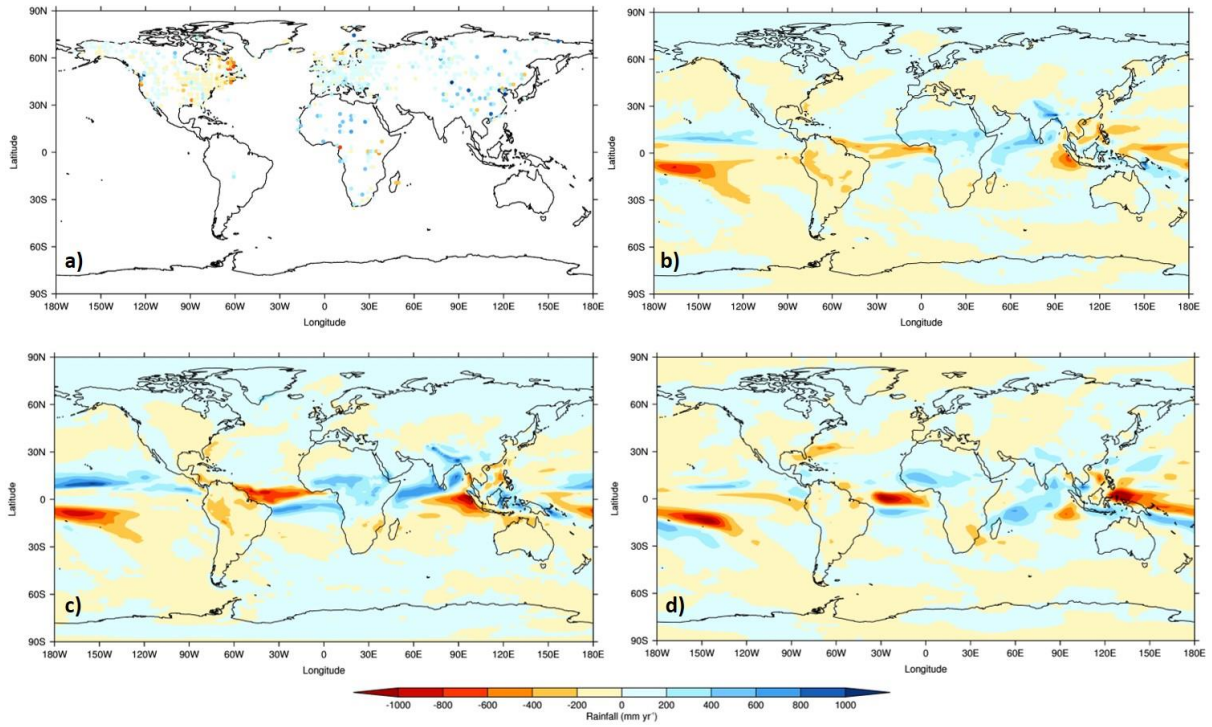
1158 MH simulations and dotted lines show LIG simulations



1159

1160 Figure 7 - Calendar adjusted mean annual surface air temperature anomalies from simulated model
 1161 data versus proxy data. Background data show simulated anomalies (MH – PI) from different
 1162 generations of the same model: a) Proxy data anomalies (MH – PI) from Bartlein et al. (2011), with
 1163 locations projected onto model grid; b) HadGEM3; c) HadGEM2-ES; d) HadCM3

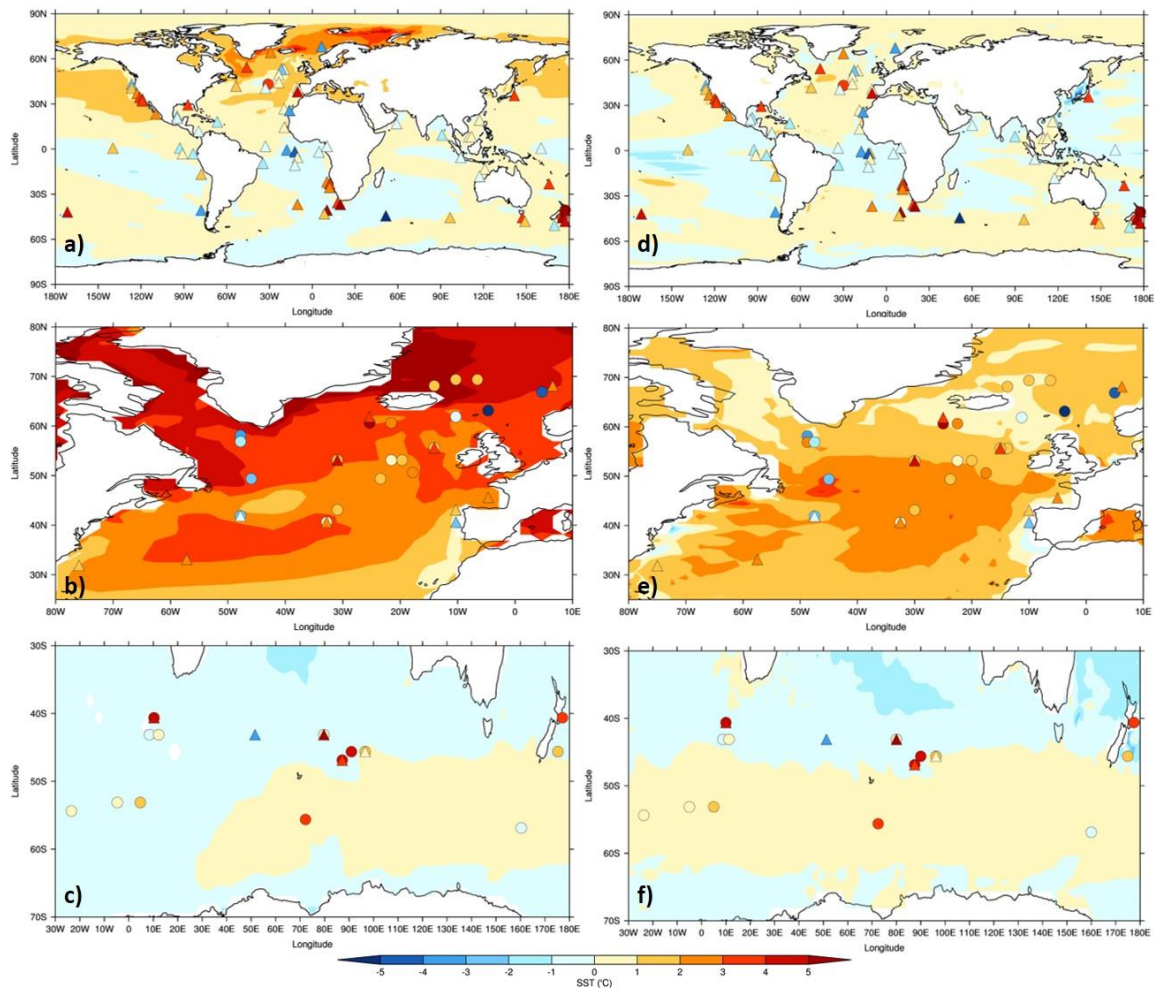
1164



1165

1166 Figure 8 - Same as Figure 7, but for rainfall anomalies

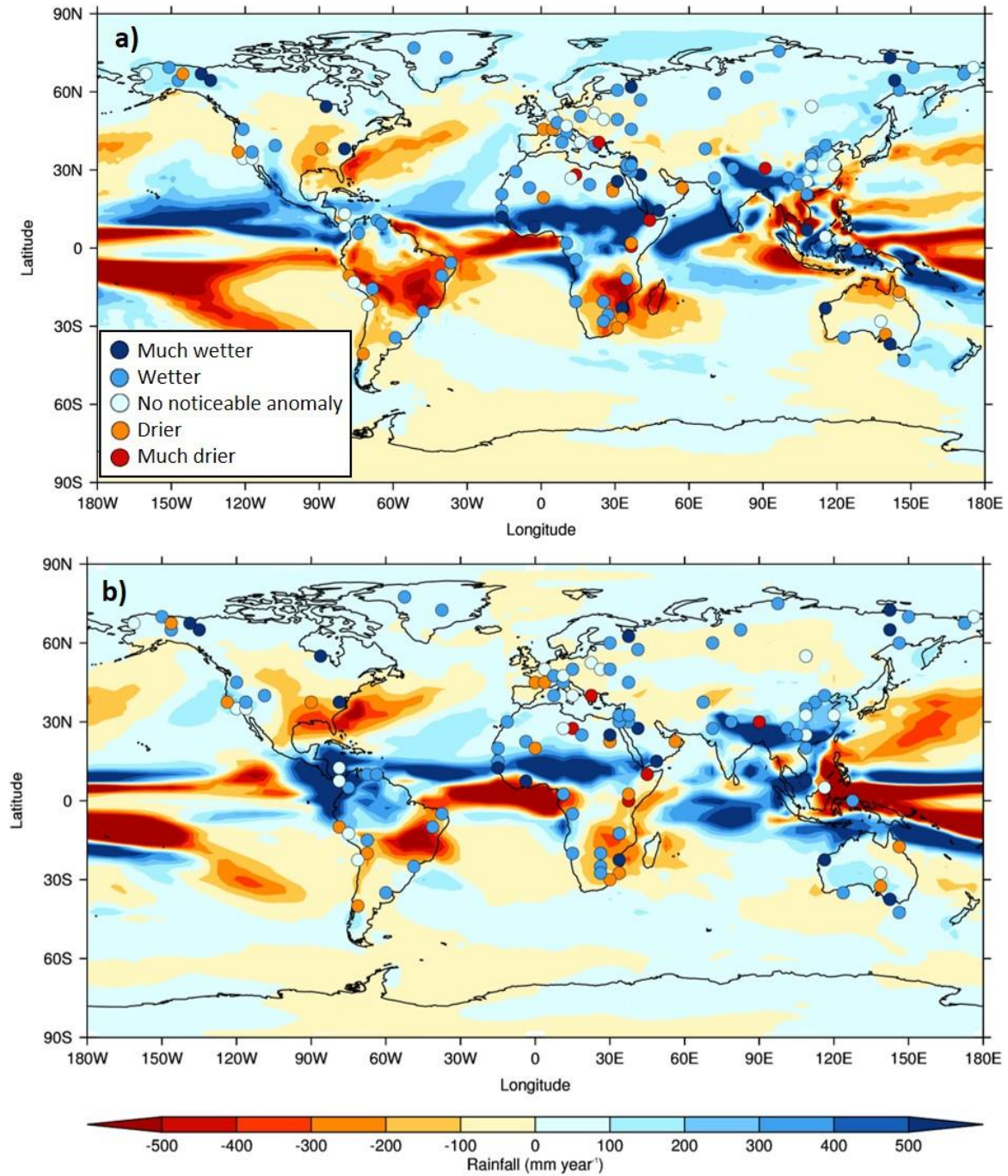
1167



1168

1169 Figure 9 - Calendar adjusted SST anomalies from model simulated data versus proxy data.

1170 Background data show simulated anomalies (LIG - PI climatology) from different generations of the
 1171 same model, circles show proxy data anomalies (LIG – preindustrial) from Capron et al. (2017) and
 1172 triangles show anomalies from Hoffman et al. (2017). Proxy data locations are projected onto model
 1173 grid: a-c) HadGEM3; d-f) HadCM3. Top row: Annual; Middle row: Northern Hemisphere summer
 1174 (JAS); Bottom row: Southern Hemisphere summer (JFM)



1175

1176 Figure 10 - Calendar adjusted annual surface rainfall anomalies from model simulated data versus
 1177 proxy data. Background data show simulated anomalies (LIG - PI climatology) from different
 1178 generations of the same model, circles show proxy data anomalies (LIG - preindustrial) from
 1179 Scussolini et al. (2019). Proxy data locations are projected onto model grid: a) HadGEM3; b)
 1180 HadCM3. Inset shows semi-quantitative scale of proxy data, adapted from Scussolini et al. (2019)
 1181